Instability and Mixing of Zonal Jets along an Idealized Continental Shelf Break

ALON STERN

Courant Institute of Mathematical Sciences, New York University, New York, New York

LOUIS-PHILIPPE NADEAU

Department of Earth, Atmospheric, and Planetary Sciences, Massachusetts Institute of Technology, Cambridge, Massachusetts

DAVID HOLLAND

Courant Institute of Mathematical Sciences, New York University, New York, New York

(Manuscript received 21 October 2014, in final form 26 May 2015)

ABSTRACT

The interaction between an Antarctic Circumpolar Current–like channel flow and a continental shelf break is considered using eddy-permitting simulations of a quasigeostrophic and a primitive equation model. The experimental setup is motivated by the continental shelf of the West Antarctic Peninsula. Numerical experiments are performed to study how the width and slope of an idealized continental shelf topography affect the characteristics of the flow. The main focus is on the regime where the shelfbreak width is slightly greater than the eddy scale. In this regime, a strong baroclinic jet develops on the shelf break because of the locally stabilizing effect of the topographic slope. The velocity of this jet is set at first order by the gradient of the background barotropic geostrophic contours, which is dominated by the slope of the topography. At statistical equilibrium, an aperiodic cycle is observed. Initially, over a long stable period, an upper-layer jet develops over the shelf break. Once the vertical shear reaches the critical condition for baroclinic instability, the jet becomes unstable and drifts away from the shelf break. The cross-shelf mixing is intrinsically linked with the jet drifting, as most of the meridional flux occurs during this instability period. Investigation of the zonal momentum budget reveals that a strong Reynolds stress divergence inversion across the jet is associated with a drifting event, accelerating one flank of the jet and decelerating the other. The hypothesis that jet drifting may be due to one flank of the jet being more baroclinically unstable than the other is tested using topographic profiles with variable curvatures.

1. Introduction

Intrusions of warm Circumpolar Deep Water (CDW) across the continental shelf break of the West Antarctic Peninsula (WAP) play a major role in maintaining the local hydrography of the region. The CDW, which originates in the Antarctic Circumpolar Current (ACC), crosses the continental shelf break of the WAP, where it becomes an important factor in balancing the ocean heat budget on the WAP continental shelf (Smith and Klinck 2002; Moffat et al. 2009). The intruding CDW is rich in nutrients and helps to sustain the large amount of biological activity in the region (Klinck et al. 2004; Hofmann et al. 2004). After crossing the continental shelf break, the intruding waters, which have a temperature exceeding 1°C, flood the WAP continental shelf, and enter the ice shelf cavities, where they cause enhanced basal melt rates (Jenkins and Jacobs 2008).

Regional models of the WAP indicate that the amount of cross-shelf exchange of CDW is modulated by large-scale atmospheric circulation patterns that control local wind directions over the continental shelf break (Dinniman et al. 2012) and is also influenced by the lateral curvature of the continental shelf (Dinniman and Klinck 2004), the presence of ocean troughs on the continental shelf (St-Laurent et al. 2013), and the amount of vertical mixing of the intruding waters with the colder surface waters (Dinniman et al. 2011).

Corresponding author address: Alon Stern, Courant Institute of Mathematical Sciences, 257 Mercer Street, New York, NY, 10012.
E-mail: alon@cims.nyu.edu

DOI: 10.1175/JPO-D-14-0213.1

Observations of the WAP have shown onshore CDW intrusion caused by eddies crossing the shelf break approximately four times a month (Moffat et al. 2009). Because of the lack of longer time series of ocean conditions, we have little information about lower-frequency variability or trends in the region.

There are a number of factors that differentiate the WAP coastal region from other regions around Antarctica: First, the southern edge of the ACC is directly in contact with the continental shelf break of WAP (Orsi et al. 1995), unlike some other parts of the Antarctic coastline, such as the Ross and Weddell Seas, where the continental shelf is isolated from the ACC by the presence of large ocean gyres and where the Antarctic slope front separates the cool waters on the continental shelf from the warmer waters offshore (Jacobs 1991). Also specific to the WAP region is a prograde (eastward) current running over the shelf break (Moffat et al. 2008), whereas a westward (retrograde) current, often referred to as the Antarctic Slope Current, is observed over the shelf break of much of the rest of Antarctica (Jacobs 1991; Whitworth et al. 1998).

In parallel to the body of literature on the continental shelf, much work has been done on zonal jets observed in β-plane channel flows (Rhines 1975; Farrell and Ioannou 2003; Srinivasan and Young 2012) and on their interaction with bottom topography. It has been shown that when an ocean jet moves over a sloping bottom topography, the growth rates of barotropic (Poulin and Flierl 2005) and baroclinic (Blumsack and Gierasch 1972; Hart 1975; Chen and Kamenkovich 2013; Poulin et al. 2014; Irwin and Poulin 2014) instabilities are strongly controlled by the gradient and orientation of the bottom topography (Benilov 2001). Furthermore, the meridional transport across the jet is related to jet meandering, which is also controlled by the bottom topography (Sokolov and Rintoul 2007; Thompson and Richards 2011). In a series of simulations particularly relevant to our study, Thompson (2010) showed that jets flowing over zonal ridges can be made to drift meridionally across background PV contours, provided the scale separating the zonal ridges is less than the Rhines scale. This observation implies that the meridional transport across the channel is modulated by the width of zonally symmetric topographic features.

Our study is an attempt to link the work done on the specific case of ACC–shelf interactions in the WAP with the more general work done on zonal jets and topography. This is done using numerical simulations with an idealized configuration of a turbulent current running parallel to a zonally symmetric continental shelf topography, which is motivated by the topography and current direction found at the continental shelf of the WAP.[1] This approach was adopted by Zhang et al. (2011) who investigated the interaction between the ACC and a prograde continental shelfbreak flow with a two-layer primitive equation (PE) isopycnic model that allows for tall topography and isopycnal outcrops. Their results show that lower-layer eddy–topography interactions inhibits the local potential vorticity flux at the edge of the shelf break, which is transmitted to the upper layer through interfacial form stress and ultimately induces the formation of a jet/front in the upper layer.

Here, we use a similar experimental setup to further study the dynamics of this shelfbreak jet. We focus on what drives the natural variability of this shelfbreak jet and how the dynamics are affected by the width and slope of the continental shelf break and the strength of the wind forcing. In most of this study we use a quasigeostrophic (QG) model, which allows us to consider a wider range of parameter regimes and study the continuous transition between β-plane channel dynamics and the particular case of a continental shelf. We focus on a parameter regime where the width of the continental shelf break is comparable to the eddy scale, for which only one strong baroclinic jet is observed over the shelf break. This shelfbreak jet displays a low-frequency intermittent variability. Most of the cross-shelf mixing coincides with jet instability events, which cause the jet to drift offshore, away from the continental shelf break. We then investigate the idea that the drifting of the jet is due to an asymmetry of the PV gradients on each side of the jet and discuss how this may be linked to enhanced cross-shelf mixing.

Section 2 gives details on the model and experimental setup and diagnostics. Section 3 presents the model results for a wide range of shelfbreak topographies and wind forcings. Section 4 focuses on shelves of intermediate width, which display a low-frequency intermittent variability. Section 5 discusses meridional jet drifting. Section 6 compares some of the key QG results to a PE model. Section 7 contains some concluding remarks.

2. Experimental design and diagnostics

a. Numerical model and experimental design

The dynamics of cross-shelf exchange are explored here using numerical experiments in a reentrant channel

---

[1] The real-world WAP continental shelf break is not zonally orientated. However, in this region, the slope of the bottom topography has a much larger effect on the background PV gradient than the gradient of the planetary rotation so that the setup can be rotated without loss of generality (as long as the mean flow runs parallel to the continental shelf break).

with a continental shelf in the south of the domain. Most of the numerical experiments are performed using a two-layer QG model. A comparison between the results of this two-layer QG model with the results of a 25-level PE model in a similar experimental setup is performed in section 6. This comparison shows that although the large-amplitude topography used here is outside of the strict asymptotic regime of the QG framework, results of the QG model are very similar to the results of the PE model, which builds our confidence in the QG model simulations presented in this study. In the following section, we describe two-layer QG model setup.

In the two-layer QG model, the potential vorticity (PV) equation in each layer can be written as

$$\frac{\partial q_1}{\partial t} + J(\psi_1, q_1) = -A_h \nabla^6 \psi_1 + \frac{\mathbf{k} \cdot \boldsymbol{\nabla} \times \boldsymbol{\tau}}{\rho_1 H_1}, \quad \text{and} \tag{1}$$

$$\frac{\partial q_2}{\partial t} + J(\psi_2, q_2) = -A_h \nabla^6 \psi_2 - r \nabla^2 \psi_2, \tag{2}$$

in which the PV in each layer is

$$q_1 = \nabla^2 \psi_1 + \beta y + F_1(\psi_2 - \psi_1) - F_0 \psi_1, \quad \text{and} \tag{3}$$

$$q_2 = \nabla^2 \psi_2 + \beta y + F_2(\psi_1 - \psi_2) + \frac{f_0 h_b}{H_2}, \tag{4}$$

where $F_0 = f_0^2/(gH_1)$; $F_1 = f_0^2/(g' H_1)$; $F_2 = f_0^2/(g' H_2)$; f_0 is the Southern Hemisphere Coriolis parameter ($f_0 < 0$); β is the northward spatial derivative of the Coriolis parameter; g is the gravitational acceleration; $g' = (g\Delta\rho)/\rho$ is the reduced gravity; H_k is the layer thickness; h_b is the bottom topography; ψ_k is the streamfunction; A_h is the biharmonic viscosity coefficient; and r is the bottom drag coefficient.

The methods used to conserve mass and momentum are described in the appendix. Free-slip and no normal flow conditions are applied at the solid walls. The model uses a third-order Adams–Bashforth time-stepping method and a multigrid method is used for the elliptic inversion. Further details of the model are described in Nadeau and Straub (2012).

In the reference simulation, the model geometry is a zonally reentrant channel, $L_x = 1200$ km long, $L_y = 1900$ km wide, and 4 km deep with a zonally symmetric hyperbolic tangent continental shelf topography

$$h_b(y) = \frac{h_0}{2} \left\{ 1 + \tanh \left[\frac{(y_0 - y)}{W} \right] \right\}, \tag{5}$$

where h_0 is the shelf height, y_0 is the latitude of the shelf break, and W is the shelfbreak width. Notice that the parameter W controls both the width and the slope of the shelf break. In the reference simulation, the center of the shelf break is $y_0 = 300$ km; the shelf height is $h_0 = 2500$ m; the layer thicknesses are $H_1 = 1000$ m and $H_2 = 3000$ m; the deformation radius $L_d = (1/f_0)\sqrt{(g' H_1 H_2)/(H_1 + H_2)} = 11.5$ km; and the grid scale used is $\Delta x = \Delta y = 3.125$ km. Each simulation is integrated for a period of 200 yr while at statistical equilibrium.

In the reference simulation, the channel is forced at the surface with a zonal wind stress profile given by

$$\tau^x(y) = \tau_0 \sin^2\left(\frac{\pi y}{L_y}\right). \tag{6}$$

In section 5, the channel is forced using an imposed background shear (Pedlosky 1979; Thompson 2010). We use constant background velocities $U_1 = U_s$ and $U_2 = 0$ to achieve a background vertical shear U_s. In this case Eqs. (1)–(2) become

$$\begin{aligned} \frac{\partial q_1}{\partial t} &+ J(\psi_1, q_1) + F_1 \psi_{1x} U_s + U_s q_{1x} + F_0 \psi_{1x} U_s \\ &= -A_h \nabla^6 \psi_1 + \frac{\mathbf{k} \cdot \boldsymbol{\nabla} \times \boldsymbol{\tau}}{\rho_1 H_1}, \quad \text{and} \end{aligned} \tag{7}$$

$$\frac{\partial q_2}{\partial t} + J(\psi_2, q_2) - F_2 \psi_{2x} U_s = -A_h \nabla^6 \psi_2 - r \nabla^2 \psi_2. \tag{8}$$

The experimental setup allows a turbulent channel flow to interact with the continental shelfbreak topography. A schematic of the experimental setup for the reference simulation is shown in Fig. 1. Model parameters are given in Table 1.

b. Diagnostics

1) BAROCLINIC INSTABILITY CRITERIA

Geostrophic eddies resulting from baroclinic instability limit the buildup of vertical shear (Johnson and Bryden 1989). Considering that the presence of the zonally symmetric bottom topography modifies locally the stability of the flow, we then expect the local condition of baroclinic instability to be a key parameter in this study. The combined effect of the eastward wind forcing and the bottom friction results in positive vertical shear in our simulations. For such a positive vertical shear, the condition for baroclinic instability is reached when the lower-layer meridional PV gradient changes sign (Pedlosky 1979). The onset of baroclinic instability then occurs when the lower-layer PV gradient is less than zero:

$$\overline{q_{2y}} = -\overline{u_{2yy}} - F_2(\overline{u_1} - \overline{u_2}) + \beta_T < 0, \tag{9}$$

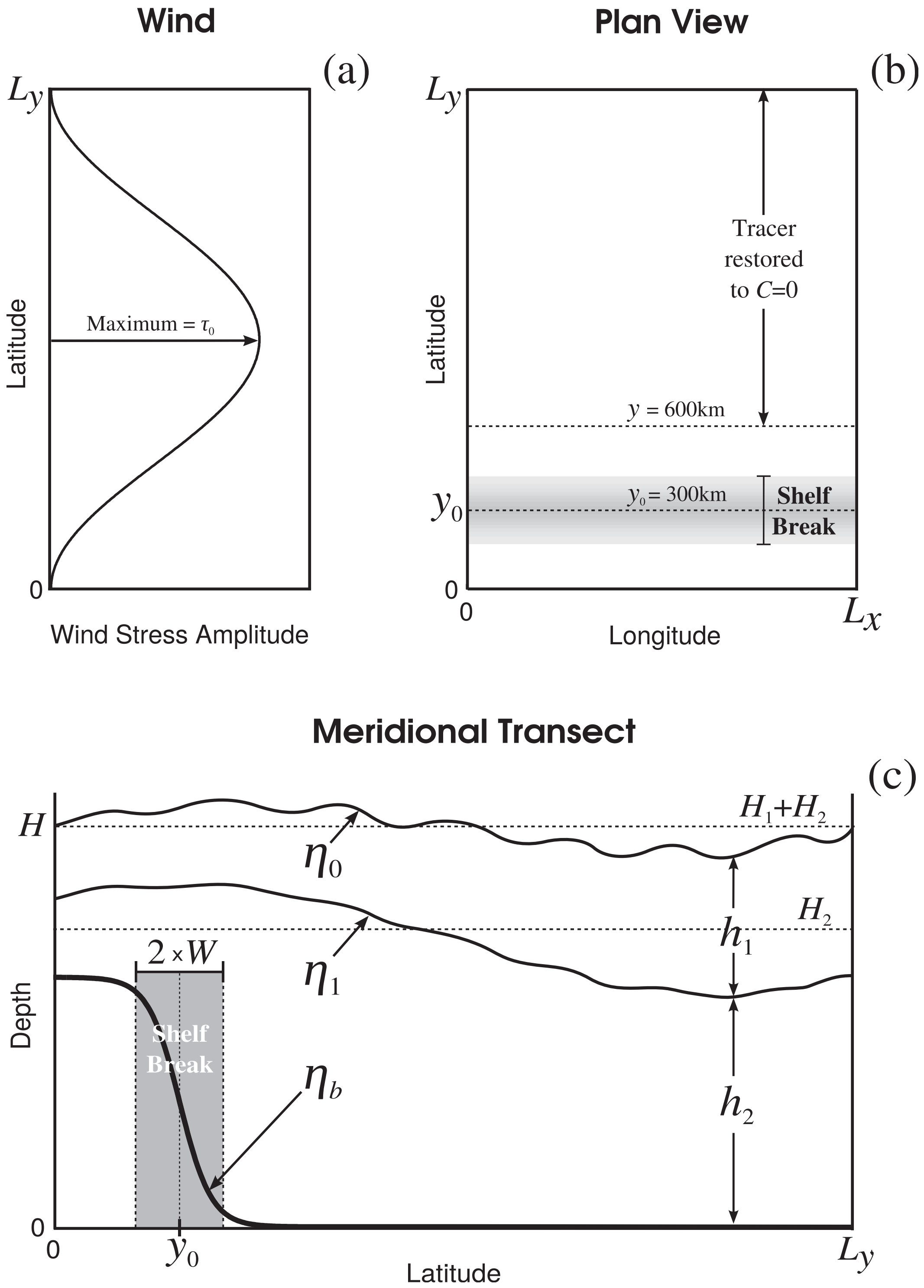

FIG. 1. (a) Wind stress amplitude vs latitude. The maximum wind stress is τ_0. (b) Plan view of experimental setup. (c) Meridional transect of the experimental setup. In (b) and (c), the shelfbreak region is shown in gray.

TABLE 1. Model parameters.

Parameter	Symbol	Value
Typical Rossby deformation radius	L_d	11.5 km
Horizontal resolution	$\Delta x = \Delta y$	3.125 km
Typical time step	Δt	1000 s
Typical spinup time	—	300 yr
Typical averaging time	—	200 yr
Length of channel	L_x	1200 km
Width of channel	L_y	1900 km
Thickness of upper layer	H_1	1000 m
Thickness of lower layer	H_2	3000 m
Gravitational acceleration	g	9.8 m s^{-2}
Typical reduced gravity	g'	0.003 m s^{-2}
Coriolis parameter	f_0	-1.3×10^{-4} s^{-1}
Beta parameter	β	1.5×10^{-11} s^{-1} m^{-1}
Reference density	ρ_1	1027 kg m^{-3}
Drag parameter	r	1.5×10^{-7}
Biharmonic dissipation coefficient	A_h	1×10^8 m^4 s^{-1}
Laplacian dissipation coefficient	κ_C	1×10^2 m^2 s^{-1}
Height of topography	h_0	2500 m
Typical shelfbreak latitude	y_0	300 km
Wind stress coefficient	τ_0	0.04, 0.08, 0.12, and 0.40 N m^{-2}
Shelfbreak width	W	$10 \le W \le 10\,000$ km

where $\overline{(\ )}$ denotes a zonal average $\oint_0^{L_x}(\ )\,dx$, and $\beta_T = \beta + [(f_0/H_2)(\partial h_b/\partial y)]$ is the effective topographic beta (Sinha and Richards 1999; Thompson 2010). We define a parameter that can be used as a criterion for stability:

$$\Gamma = (u_1 - u_2) + \frac{u_{2yy}}{F_2}. \tag{10}$$

The critical instability condition Eq. (9) then simply becomes $\Gamma > \beta_T/F_2$. For the topographic shelf given by Eq. (5), the maximum value of β_T/F_2 occurs at the center of the shelf break y_0 and is given by $\max(\beta_T/F_2) = \{\beta - [(f_0/H_2)(h_0/2W)]\}/F_2$. The value of Γ observed over the shelf break then becomes a useful metric to classify our experimental results: $\Gamma \sim \max(\beta_T/F_2)$ corresponds to criticality, $\Gamma < \max(\beta_T/F_2)$ corresponds to subcriticality, and $\Gamma > \max(\beta_T/F_2)$ corresponds to supercriticality.

2) CROSS-SHELF EXCHANGE DIAGNOSTICS

Two measures of cross-shelf exchange are used in this manuscript: 1) the PV flux across the shelfbreak center and 2) the flux of passive tracer across the shelfbreak center.

1) The zonally averaged meridional eddy PV flux $\overline{q'_k v'_k}$, evaluated at the shelfbreak center latitude $y_0 = 300$ km, is used as a first measure of the cross-shelf mixing. Here, $\overline{(\ )}$ is the zonal mean, and $(\ )'$ is the deviation from the zonal mean.[2] Neglecting dissipation and integrating Eqs. (1) and (2) over the area south of a given latitude y gives

$$\frac{1}{L_x}\frac{\partial}{\partial t}\oint_0^{L_x}\int_0^y q_1\,dA = -\overline{v'_{g1}q'_1} - \frac{\overline{\tau}}{\rho_1 H_1}, \quad \text{and} \tag{11}$$

$$\frac{1}{L_x}\frac{\partial}{\partial t}\oint_0^{Lx}\int_0^y q_2\,dA = -\overline{v'_{g2}q'_2} + r\overline{u_{g2}}. \tag{12}$$

The terms on the right-hand side of Eqs. (11) and (12) are evaluated at the latitude y, and $u_g = -\partial\psi/\partial y$ and $v_g = \partial\psi/\partial x$ are the first-order geostrophic horizontal velocities. Letting $y = y_0$ in Eqs. (11) and (12) gives the evolution of PV over the continental shelf.

2) A passive tracer in each layer is advected by the flow according to the equation

$$\frac{\partial C_k}{\partial t} + J(\psi_k, C_k) = \kappa_C \nabla^2 C_k, \tag{13}$$

where $\kappa_C = 10^2$ m^2 s^{-1} is the dissipation coefficient. The value of the tracer is fixed at $C = 1$ on the southern boundary ($y = 0$ km), and $C = 0$ for $y \ge 600$ km. This Dirichlet boundary condition allows tracer to flux into the domain in the south and out of the domain at $y = 600$ km. The tracer is initialized to vary linearly from one to zero over the interval [0, 600 km]. The zonally averaged meridional tracer flux through the latitude $y_0 = 300$ km (shelfbreak center) is used as a second measure for cross-shelf mixing.

3. The effect of the shelfbreak width and slope

a. *Phenomenology*

We begin our investigation by performing a set of experiments using the reference setup of Fig. 1 and varying the parameter W [see Eq. (5)], which controls the width and slope of the continental shelf break. Figure 2 shows the Hovmöller diagrams of the zonal-mean upper-layer zonal velocity for various values of the shelfbreak width W and two values of the wind stress amplitude τ_0. Experiments can be classified in terms of the number of jets that develop over the shelf

---

[2] In our experimental setup, the zonally averaged meridional velocity is zero, $\overline{v_k} = 0$, which implies that the zonally averaged meridional PV flux only has a contribution from eddy terms, that is, $\overline{q_k v_k} = \overline{q'_k v'_k}$.

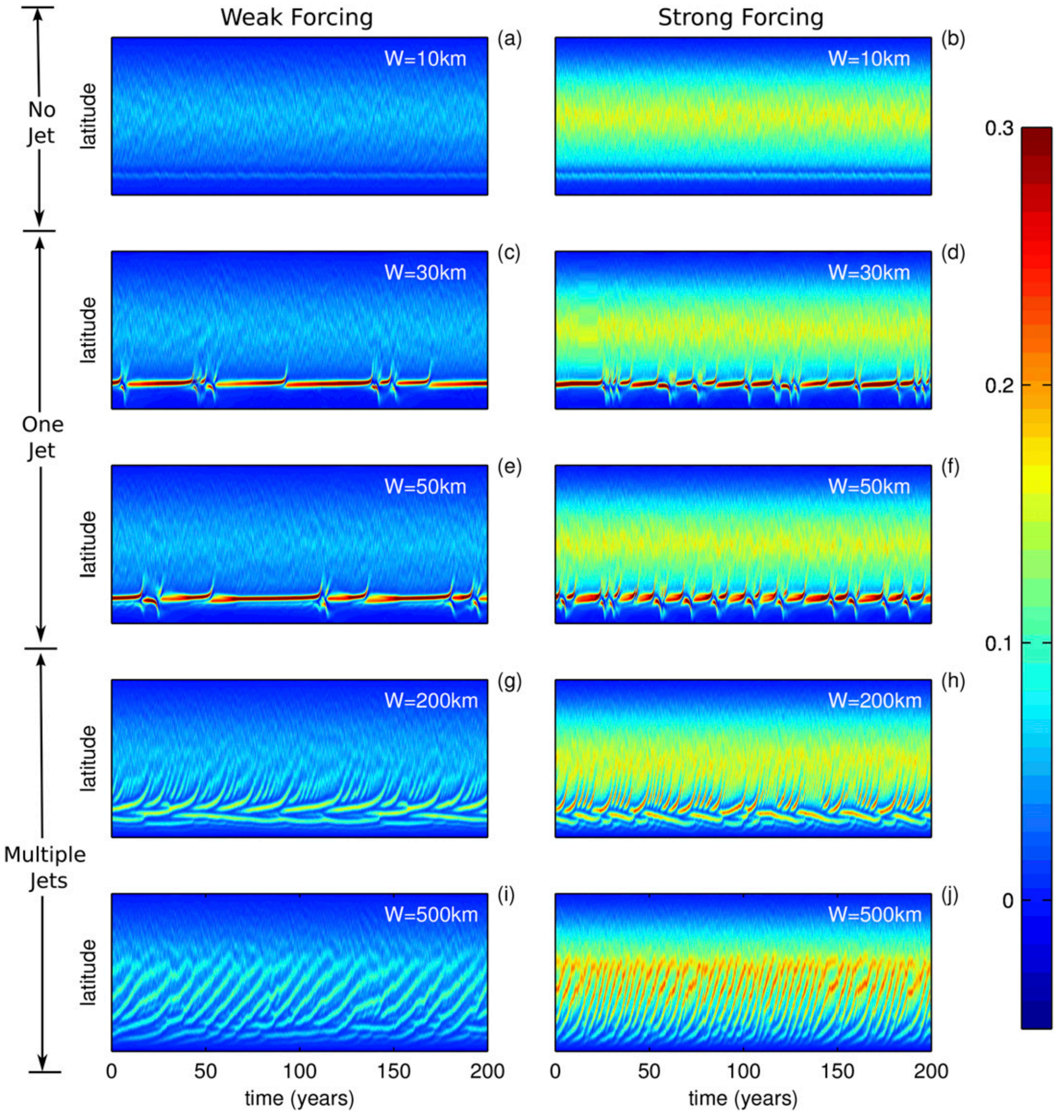

FIG. 2. Hovmöller diagrams of the upper-layer zonally averaged zonal velocity are shown for different wind forcings and different shelfbreak widths. Wind forcings (left) $\tau_0 = 0.04\,\mathrm{N\,m^{-2}}$ and (right) $\tau_0 = 0.12\,\mathrm{N\,m^{-2}}$. (top to bottom) Shelfbreak width parameters $W = 10$, 30, 50, 200, and 500 km are shown.

break: (i) for $W \lesssim 23$ km, no jet forms over the shelf break; (ii) for $23 \lesssim W \lesssim 100$ km, we observe a unique shelfbreak jet that remains stationary for a number of years before becoming unstable and drifting away from the shelf break; and (iii) for $W \gtrsim 100$ km, multiple jets form over the shelf break. In this last regime, the shelfbreak jet does not remain stationary at any time and instead is constantly drifting. The drift direction in this regime is primarily northward, although some southward drifting jets are observed for narrower shelf breaks. The jets are most clearly seen in the upper layer and have much decreased magnitude in the lower layer.

Figure 3a shows the maximum value of the stability criterion Γ [see Eq. (10)] obtained in our simulations for different shelfbreak widths and wind forcings. The dashed line shows the condition of baroclinic instability at the center of the shelf break: $\max(\beta_T/F_2) = \{\beta - [(f_0/H_2)(h_0/2W)]\}/F_2$. Figure 3a shows that the classification defined above for each of the three regimes also applies roughly to the stability criterion. The subcritical regime $[\Gamma_{\max} < \max(\beta_T/F_2)]$ occurs for $W \lesssim 23$ km and fits approximately the regime where no jet is observed on the shelf break. Similarly, the critical regime $[\Gamma_{\max} \sim \max(\beta_T/F_2)]$ corresponds approximately to the one jet regime observed for $23 \lesssim W \lesssim 100$ km.

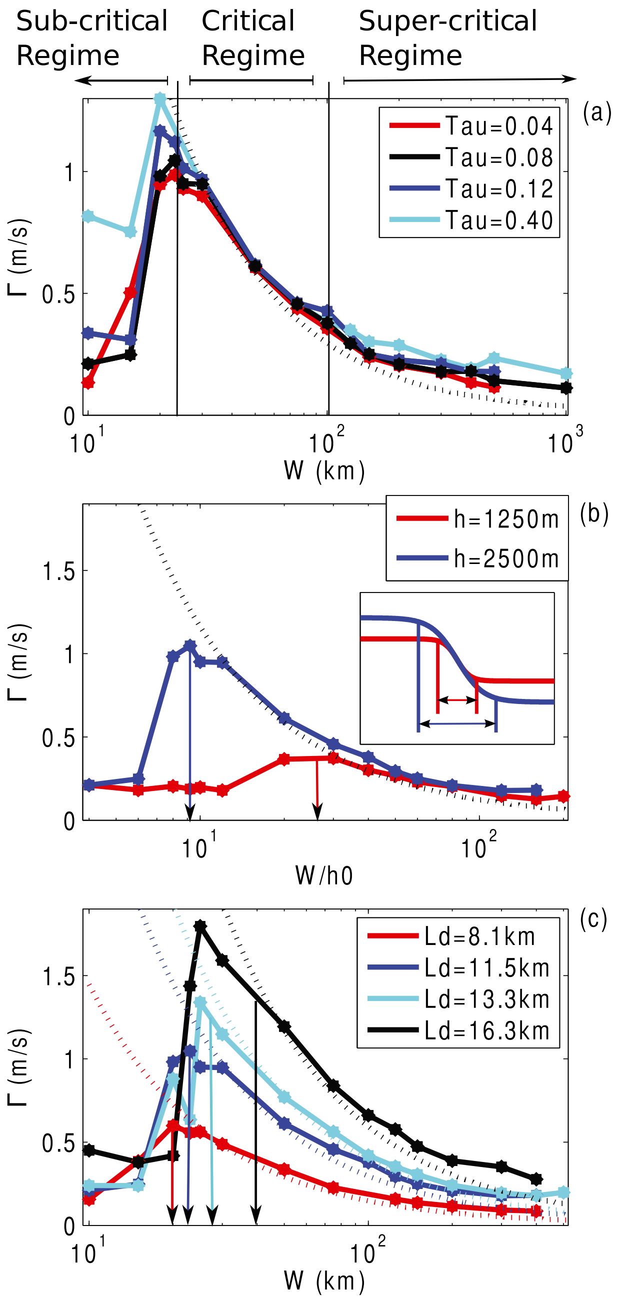

FIG. 3. (a) Maximum value of the stability criterion $\Gamma_{\max}$ over the shelfbreak region for simulations using different shelfbreak widths W and wind forcings τ_0. (b) Maximum value of $\Gamma_{\max}$ for simulations using different shelfbreak widths W and continental shelf heights h_0. Note that the x axis is W/h_0. An example of the topography used in this experiment is shown in the inset figure. (c) Maximum value of $\Gamma_{\max}$ for different shelfbreak widths W and deformation radii L_d. The maximum normalized effective topographic beta $\max(\beta_T/F_2)$ is shown by dashed lines in each panel and indicates the necessary condition for baroclinic instability at the latitude y_0. Simulations in (a) and (b) use deformation radius $L_d = 11.5$ km. Simulations in (b) and (c) use wind forcing $\tau_0 = 0.08\,\mathrm{N\,m^{-2}}$. Downward arrows in (b) and (c) show the approximate W that mark the border between the subcritical and critical regimes. The arrows have been positioned between data points when the smaller W simulation was in the subcritical regime and larger W simulation was in the critical regime.

In this regime, $\Gamma_{\max}$ is set by the slope of the bottom topography and is independent of the wind stress. Finally supercriticality [$\Gamma_{\max} > \max(\beta_T/F_2)$] is observed in the multiple jet regime ($W > 100$ km).

In the following, we focus on what sets the length scales that separate the three regimes. We argue that the lower bound of the critical regime occurs when the shelfbreak width becomes smaller than the eddy scale. The upper bound is not as sharp as the lower bound and occurs when the slope of the shelf break becomes small enough to allow vertical shear to rise above the condition of baroclinic instability.

1) TRANSITION TO SUBCRITICAL REGIME

We first focus on the transition between the no jet and the one jet regime at $W \sim 23$ km. Equation (5) shows that the actual width of the shelf break is approximately $2W$ (see also Fig. 1). For $W = 23$ km, the shelfbreak width is then 46 km, which is approximately 4 times the deformation radius. We refer to this length scale as the eddy scale, $L_e \sim 4L_d = 46$ km. This suggests that it is the eddy scale that defines the boundary between the subcritical and critical regimes. Since W alters both the slope and the width of the shelf break, we perform two sets of simulations to decouple these effects. The first set of experiments is used to show that the boundary occurs at a critical width rather than a critical slope. The second set of experiments show that this critical width corresponds to the eddy scale for a range of deformation radii.

The inset panel of Fig. 3b shows that by varying the height of the shelf h_0, one can design experiments with variable shelfbreak width but equal slope at the center of the shelf break y_0. For such experiments, the parameter W/h_0 controls the topographic slope at $y = y_0$. Figure 3b shows the maximum value of Γ as a function of W/h_0 for simulations using two different shelf heights. The dashed line corresponds to the instability threshold at the center of the shelf break: $\max(\beta_T/F_2) = \{\beta - [(f_0/H_2)(h_0/2W)]\}/F_2$. Each simulation is performed using a fixed deformation radius $L_d = 11.5$ km and a fixed wind stress $\tau_0 = 0.08\,\mathrm{N\,m^{-2}}$. Figure 3b shows that the transition to subcriticality occurs at different slopes for simulations using different values of h_0. Moreover, when results are rescaled by h_0, the transition to subcriticality occurs approximately at the same width for both shelf heights (not shown). This suggests that it is the width of the shelf break (rather than the slope) that sets the scale of the subcritical regime.

In the second set of experiments, we vary the deformation radius. Figure 3c shows the maximum value of Γ as a function of W for different deformation scales L_d. The value of $\max(\beta_T/F_2)$ is plotted using dashed lines for each of the deformations scales. Despite the fact that the transition to subcriticality becomes more abrupt for increasing L_d, results show that the upper bound of the subcritical region increases with the deformation radius and is approximately given by the eddy scale. For example, the transition occurs at $W \sim 20\,\mathrm{km}$ for $L_d = 8.1\,\mathrm{km}$ and $W \sim 40\,\mathrm{km}$ for $L_d = 16.3\,\mathrm{km}$. This further reinforces the idea that the flow becomes subcritical when the width of the shelf break becomes smaller than the eddy scale.

While the transition between the subcritical and critical regimes is fairly sharp, there exist a small range of shelfbreak widths near the boundary of the subcritical and critical regimes where a weak jet occasionally forms over the shelf break and where $\Gamma_{\max}$ increases with W. In this transitional range, the jet flanks are not entirely over the shelf break and become unstable before the jet center, which may explain why they do not reach criticality.

2) TRANSITION TO SUPERCRITICAL REGIME

In the flat bottom region north of the shelf break, criticality is observed with very weak winds only. From this weak forcing, increasing the winds also increases the vertical shear,[3] and the flow becomes supercritical. The occurrence of a region of critical baroclinic instability in the channel is due to the strong topographic slope that stabilizes the flow over the shelf break. Thus, decreasing topographic slope (increasing W), the vertical shear can eventually exceed the critical condition for baroclinic instability. This explains why transition to supercriticality is gradual, unlike the sharp transition between the subcritical and critical regimes. In the critical regime, $\Gamma_{\max}$ is set by the slope of the bottom topography and is independent of the wind forcing, while in the supercritical regime, $\Gamma_{\max}$ increases with the wind forcing (Fig. 3a). The boundary between the critical and supercritical regimes occurs at large W and depends on the slope of the bottom topography rather than the width of the shelf break. In the supercritical regime in our experiments, the length scale of the shelf break is much larger than the eddy scale, and its slope is nearly linear such that the dynamics are very similar to those of a beta-plane turbulent flow. This regime is characterized by the occurrence of multiple jets and has been studied extensively in other studies (e.g., Rhines 1975; Farrell and Ioannou 2003; Thompson 2010; Srinivasan and Young 2012). Notice, however, that it is possible to obtain multiple jets in a near-critical state at very weak forcing. Thus, the transition from a single jet to multiple jets is not necessarily correlated with the transition from the critical to the supercritical regime.

The above results are summarized in Fig. 4, which shows the criticality ratio $\Gamma_{\max}/\max(\beta_T/F_2)$ for simulations using different values of W and deformation scales, for a wind stress amplitude $\tau_0 = 0.08\,\mathrm{N\,m^{-2}}$. The black dots in Fig. 4 indicate simulations that were performed. A black line is plotted showing the eddy scale $L_{\mathrm{eddy}} \sim 4L_d$. For W smaller than the eddy scale, the shelfbreak flow is subcritical $[\Gamma_{\max}/\max(\beta_T/F_2)] < 1$. In this regime no jet formation is observed over the shelf break, and the vertical shear is small. For W slightly larger than the eddy scale, the flow remains close to the condition of baroclinic instability $[\Gamma_{\max}/\max(\beta_T/F_2)] \sim 1$, and the maximum shear is strongly controlled by the slope of the bottom topography. For larger W, the slope of the shelf break gets smaller and the shelfbreak flow becomes supercritical: $[\Gamma_{\max}/\max(\beta_T/F_2)] > 1$. While the transition between the subcritical regime and critical regime is due to the width of the shelf break, the transition between the critical regime and supercritical regime is due to the slope of the shelf break.

b. *Baroclinic or barotropic instability?*

Figure 2 shows that zonal jets develop on the shelf break for widths larger than the eddy scale. When these jets become unstable, a train of coherent vortices is created over the shelf break (not shown), and the jet drifts away from the shelfbreak center with a velocity that depends on the width parameter W and the wind stress amplitude τ_0. One can ask if these dynamics are specific to those of a baroclinic system or if this instability and drifting could be explained from a barotropic analysis. Here, we address this question by comparing baroclinic and barotropic instability conditions.

Results for a simulation typical of the one jet regime, using $W = 50\,\mathrm{km}$, $\tau_0 = 0.08\,\mathrm{N\,m^{-2}}$, and $L_d = 11.5\,\mathrm{km}$, are shown in Fig. 5. Figures 5a and 5b show the Hovmöller diagram of the zonal-mean upper-layer zonal velocity and the vertical shear averaged over the shelfbreak region. The vertical shear accumulates over a long period during which the jet is stable. This is followed by a sharp decrease in shear, as the jet begins to drift.

Figure 5c show the time series of the lower-layer PV gradient $\partial q_2/\partial y$ and the barotropic PV gradient $\partial q_B/\partial y$ averaged over the shelfbreak region. Recall that in our system baroclinic instability occurs for $\partial q_2/\partial y < 0$, whereas barotropic instability occurs for $\partial q_B/\partial y < 0$. The lower-layer PV gradient decreases steadily during periods of vertical shear accumulation. The jet instability occurs when the lower-layer PV gradient

---

[3] In a flat bottom channel, geostrophic eddies are believed to offset the increasing winds only partially (Johnson and Bryden 1989), such that the baroclinic shear is not totally saturated.

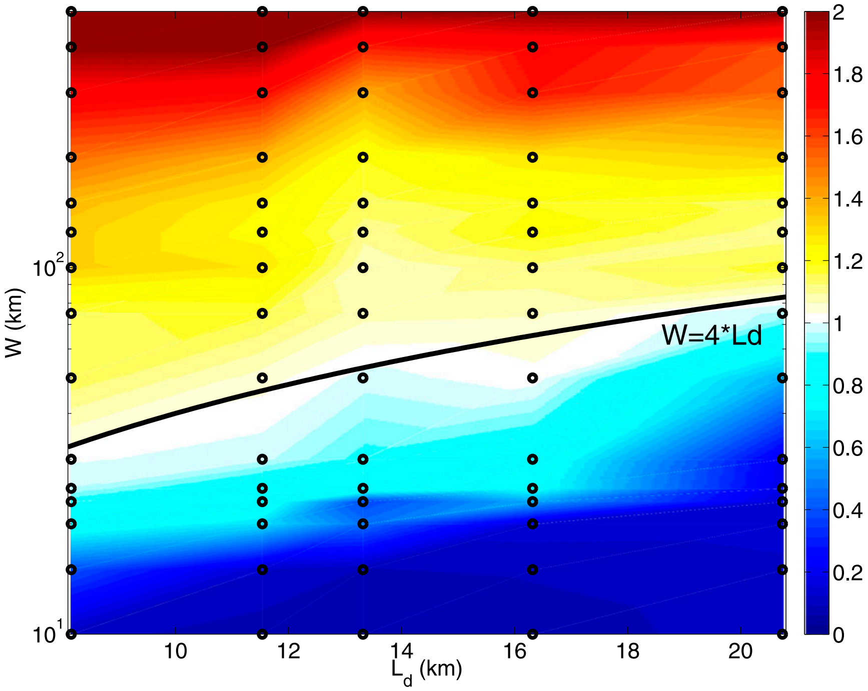

FIG. 4. Maximum value of the criticality ratio $\Gamma_{\max}/[\max(\beta_T/F_2)]$ observed during 200-yr simulations using different shelfbreak widths W and different deformation radii L_d. The various simulations are indicated by circles. The flow is critical when $\Gamma_{\max}/[\max(\beta_T/F_2)] \sim 1$, subcritical when $\Gamma_{\max}/[\max(\beta_T/F_2)] < 1$, and supercritical when $\Gamma_{\max}/[\max(\beta_T/F_2)] > 1$. The line $W = 4L_d$ has been included for reference and marks the transitional width where the shelf is no longer wide enough to support a jet and the flow becomes subcritical. For very large values of W, the flow is supercritical.

becomes negative[4] at a time where the barotropic PV gradient only starts to decrease. The onset of drifting also coincides approximately with the vertical shear reaching the condition for baroclinic instability given by the Phillips model[5] (Phillips 1954; Pedlosky 1979), shown with a dashed line in Fig. 5b. As such, Fig. 5c demonstrates that the flow becomes baroclinically unstable before becoming barotropically unstable. This suggests that baroclinic instability is a key to describing the dynamics of the shelfbreak region.

c. *Cross-shelf mixing associated with instability events*

Time series of the upper-layer meridional PV flux and passive tracer flux are shown in Figs. 5d and 5e, respectively. Each flux is sampled across the shelfbreak center y_0. Mixing is very weak during periods where the jet is stable. The magnitude of both PV and tracer fluxes increases significantly when the jet becomes unstable. The lower-layer meridional PV flux and tracer flux behave in a similar way but with much smaller magnitudes (not shown).[6] Most of the mixing occurs in short periods corresponding to the instability of the jet. In the following, we refer to these as mixing events or instability events. During these events, the combined effect of reaching a maximum in PV flux (Fig. 5d), simultaneous with a minimum in PV gradient (Fig. 5b), results in large-eddy diffusivity over the shelfbreak region (not shown).

To understand how the width parameter affects the magnitude of the mixing events, we show in Figs. 6a and 6b

---

[4] In Fig. 5c, $\partial q_2/\partial y$ is averaged over the shelf break and appears to only reach zero but actually becomes negative at the shelfbreak center.

[5] The stability criterion Γ [in Eq. (10)] is dominated by the vertical shear, and the curvature term u_{yy} plays a secondary role. As such, the Phillips model's condition, which ignores the curvature term, predicts reasonably well the onset of the instability.

[6] The reduced fluxes in the lower layer result from the lower-layer PV gradient being smaller than that of the upper layer. In the WAP, observations show that the amplitude of the PV gradients is largest in the CDW layer (Moffat et al. 2009). The enhanced upper-layer PV gradient and PV fluxes thus suggest that the upper layer in the two-layer QG simulations is representative of the CWD layer.

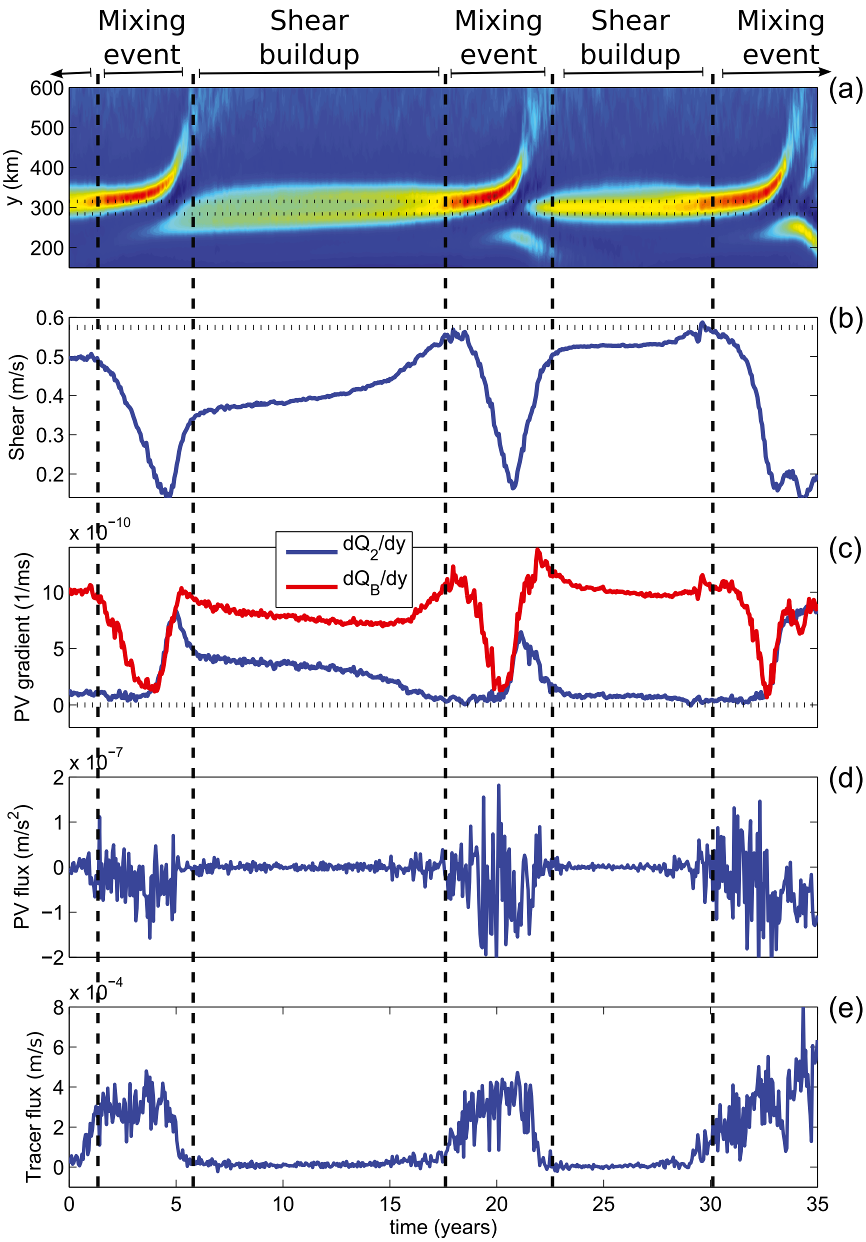

FIG. 5. (a) Hovmöller diagram of the upper-layer zonally averaged zonal velocity in the southern half of the domain. Time series of the (b) vertical shear, (c) lower-layer PV gradient and barotropic PV gradient, (d) upper-layer meridional PV flux, and (e) upper-layer tracer flux, averaged over the shelfbreak region. Quantities shown in (b),(c),(d), and (e) are averaged between $y = 280$ km and $y = 320$ km [marked by dotted lines in (a)].

the maximum of the recorded upper-layer cross-shelf PV flux and tracer flux over the shelf break, as a function of W. The lower-layer fluxes yield qualitatively similar behavior but have much smaller amplitudes (not shown). The size of the mixing events increases with wind forcing. This is especially clear for $W > 23$ km, when jets do form on the shelf. Both the PV and tracer fluxes show that mixing events peaks at $W \sim 23$ km. The mixing maximum observed in Fig. 6 corresponds roughly to the peak observed for the maximum of the stability criterion $\Gamma_{\max}$ in Fig. 3a. Since in most of our experiments $\Gamma_{\max}$ is dominated by the vertical shear, this suggests that the magnitude of a given cross-shelf mixing event is closely related to the vertical shear recorded over the shelf break before this event. Interestingly, the strong dependence of the upper-layer PV gradient on W

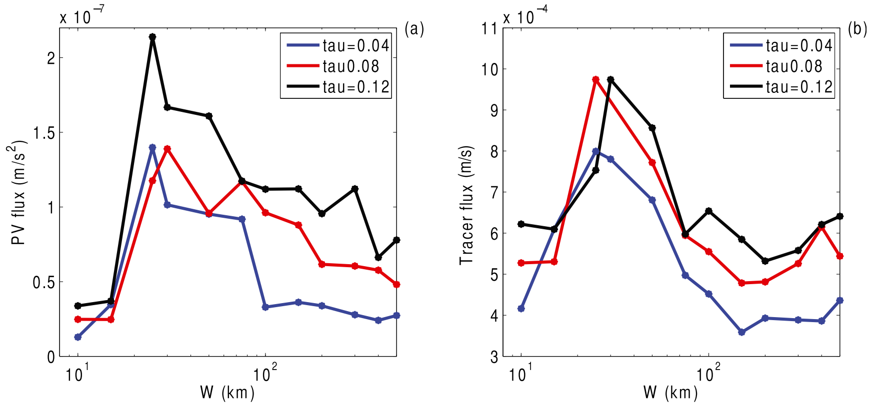

FIG. 6. (a) Maximum magnitude of the upper-layer meridional PV flux and (b) maximum upper-layer tracer flux, at the shelfbreak latitude y_0, for different values of the shelfbreak width parameter W and wind forcing τ_0.

implies that the maximum eddy diffusivity over the shelf break during an instability increases steadily with W and does not have a maximum at $W \sim 23$ km (not shown).

4. Intermittent critical regime

Mixing associated with the instability events is maximal when the shelfbreak width is of the same order of magnitude (or slightly bigger) than the eddy scale: $2W \gtrsim L_{\mathrm{eddy}}$. In this regime, the strong topographic slope allows for high local values of vertical shear, but the narrow shelfbreak region can support one jet only. This jet becomes unstable in an aperiodic manner, whenever the stability condition Γ reaches the critical condition for baroclinic instability.

In the WAP region, most of the continental shelf break has a scale on the order of 50 km, with a deformation radius of between 5 and 10 km. Figure 3c then suggests that the flow is likely to be in the critical regime. Thus, because this regime may be closer to observations and because it has not been studied as extensively as the case of wider sloping regions with multiple jets, we now focus on the dynamics of this specific regime referred to as the "intermittent critical regime." Throughout this section, a single reference simulation is considered, with $W = 50$ km and $\tau_0 = 0.08\,\mathrm{N\,m^{-2}}$, which is a typical example of a simulation in this parameter regime.

a. Spinup from rest

Results obtained for the channel spinup of the reference simulation are shown in Fig. 7. Figures 7a and 7b show Hovmöller diagrams of the zonal-mean upper-layer zonal velocity and PV, respectively. In the flat bottom region north of the shelf break, the channel flow is fully spun up after approximately 50 yr. In contrast, the shelfbreak flow has a much longer equilibration period of almost 300 yr. A sharp PV barrier and associated zonal jet forms and strengthens over the continental shelf break during this equilibration period. Figures 7c and 7d show time series of different zonally averaged terms of the PV budget [see Eqs. (12) and (11)] evaluated at the shelf break at latitude: the upper-layer meridional PV flux $q_1'v_1'$, the wind forcing $\tau/(\rho H_1)$, the lower-layer meridional PV flux $q_2'v_2'$, and the bottom friction $-ru_{g2}$. While the jet is stable, the PV flux remains close to zero in both layers. During these stable periods, the positive wind forcing slowly builds negative PV on the continental shelf in the upper layer, whereas the bottom friction builds positive PV on the continental shelf in the lower layer. As discussed earlier in Fig. 5, when the lower-layer PV gradient becomes negative, the jet becomes unstable. A strong PV flux is associated with the jet instability and acts in the opposite direction as the wind in the upper layer and the bottom friction in the lower layer. Once the model is fully spun up, instability events are sufficiently large that the time-mean PV flux balances the wind forcing in the upper layer and the friction in the lower layer.

WHY DO JETS FORM OVER THE SHELF BREAK?

In our simulations, the time-averaged vertical shear is the dominant contribution to the upper-layer PV gradient $\partial q_1/\partial y \sim F_1(u_1 - u_2)$ [from Eq. (3)]. Since the lower-layer velocity u_2 is small and essentially set by the bottom drag, the magnitude of the upper-layer PV gradient thus gives an estimate of the strength of the surface shelfbreak jet. To obtain an expression of this upper-layer PV gradient that includes the influence of the topography, we first consider the zonally averaged barotropic PV equation

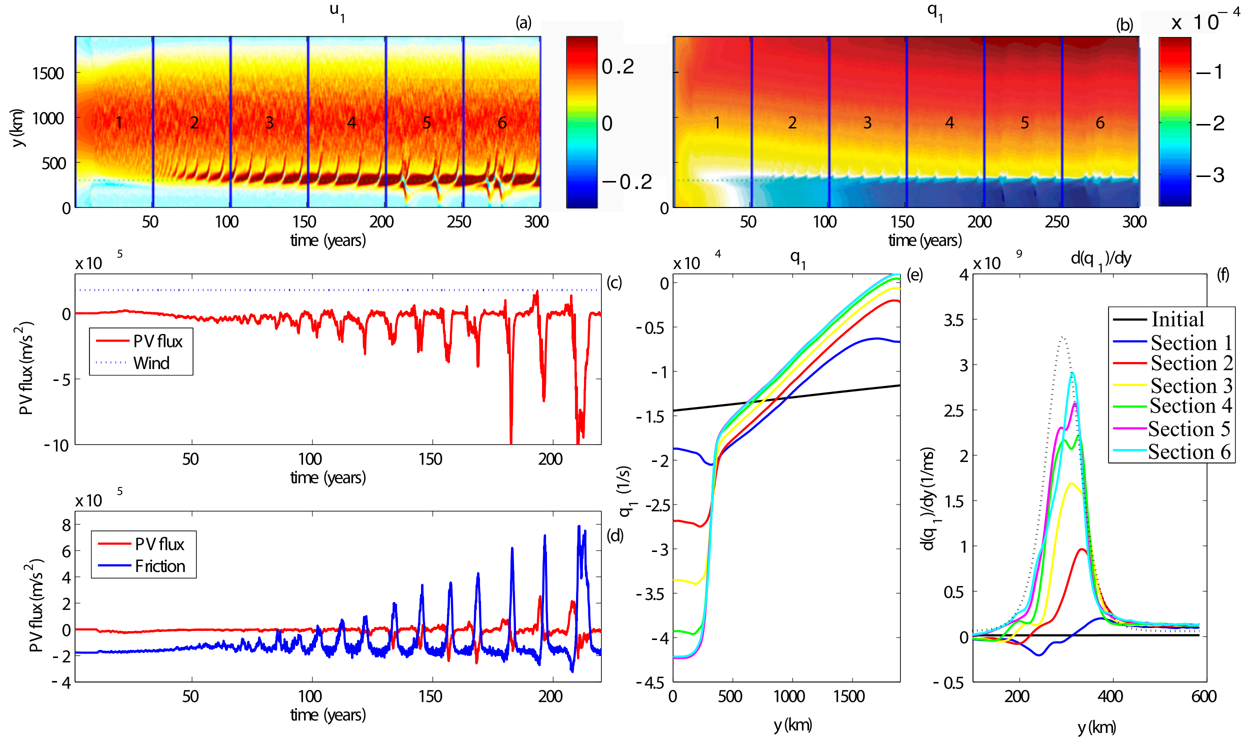

FIG. 7. Hovmöller diagram of the upper-layer zonally averaged (a) zonal velocity and (b) PV from a spinup of the reference configuration ($\tau_0 = 0.08\,\mathrm{N\,m^{-2}}$, $W = 50\,\mathrm{km}$) initially at rest. Time series of the zonally averaged (c) upper-layer meridional PV flux $\overline{q_1'v_1'}$ and the wind forcing $\overline{\tau}/(\rho H_1)$ and (d) lower-layer meridional PV flux $\overline{q_2'v_2'}$ and drag $-ru_{g2}$ during spinup, evaluated at the shelf break at latitude y_0y_0. Time-averaged upper-layer (e) PV and (f) PV gradient during six different stages of the spinup process. The time averages are taken over the six time intervals shown in (a). The dashed line in (f) shows the upper-layer effective beta β_{T1}, which is the analytic estimate of the equilibrium upper-layer PV gradient [see Eq. (15)].

$$H_1\overline{q_1} + H_2\overline{q_2} = H_1\overline{\psi_{1yy}} + H_2\overline{\psi_{2yy}} + (H_1 + H_2)\beta y - \frac{f_0}{g}\overline{\psi_1} + f_0 h_b\,, \tag{14}$$

obtained by combining Eqs. (3) and (4). Coming back to Fig. 5c, we now take advantage of the fact that $\partial q_2/\partial y$ is close to zero on average (i.e., the flow is close to criticality). Then, taking the y derivative of Eq. (14), assuming that $\partial q_2/\partial y \sim 0$, and neglecting the terms associated with the free surface and relative vorticity gives

$$\frac{\partial\overline{q_1}}{\partial y} \sim \left(\frac{H_1 + H_2}{H_1}\right)\beta + \frac{f_0}{H_1}\frac{\partial h_b}{\partial y} = \beta_{T1}\,, \tag{15}$$

where β_{T1} is the upper-layer topographic beta. Notice that this is equivalent to the gradient of the background barotropic geostrophic contours, which is dominated by the topographic slope over the shelf break.

Over the shelf break, where the topographic term dominates β_{T1}, Eq. (15) implies that the vertical shear can be approximated as $(u_1 - u_2) \sim (1/F_1)(f_0/H_1)(\partial h_b/\partial y)$. This expression can be rewritten as

$$\frac{\partial}{\partial y}\left[\frac{f_0}{g'}(\psi_2 - \psi_1)\right] \sim \frac{\partial h_b}{\partial y}\,,$$

which shows that the layer interface $\eta_1 = (f_0/g')(\psi_2 - \psi_1)$ is adjusting to be parallel to the bottom topography.

Figures 7e and 7f show the zonally averaged profiles of the upper-layer PV and PV gradient, averaged for periods of 50 yr corresponding to sections 1 to 6 (see Figs. 7a,b). The upper-layer topographic beta β_{T1} is shown by the dashed line in Fig. 7f. During spinup, in the upper-layer, negative PV builds up on the continental shelf until the PV gradient approaches β_{T1}. The fact that β_{T1} is equivalent to the gradient of the background barotopic geostrophic contours suggests that the development of the shelfbreak jet is primarily due to barotropic dynamics.[7] However, by maintaining an important

---

[7] A similar result was found by Boland et al. (2012), who showed that in a two-layer QG model where the upper- and lower-layer PV gradients have different orientations, jets follow the barotropic PV gradient.

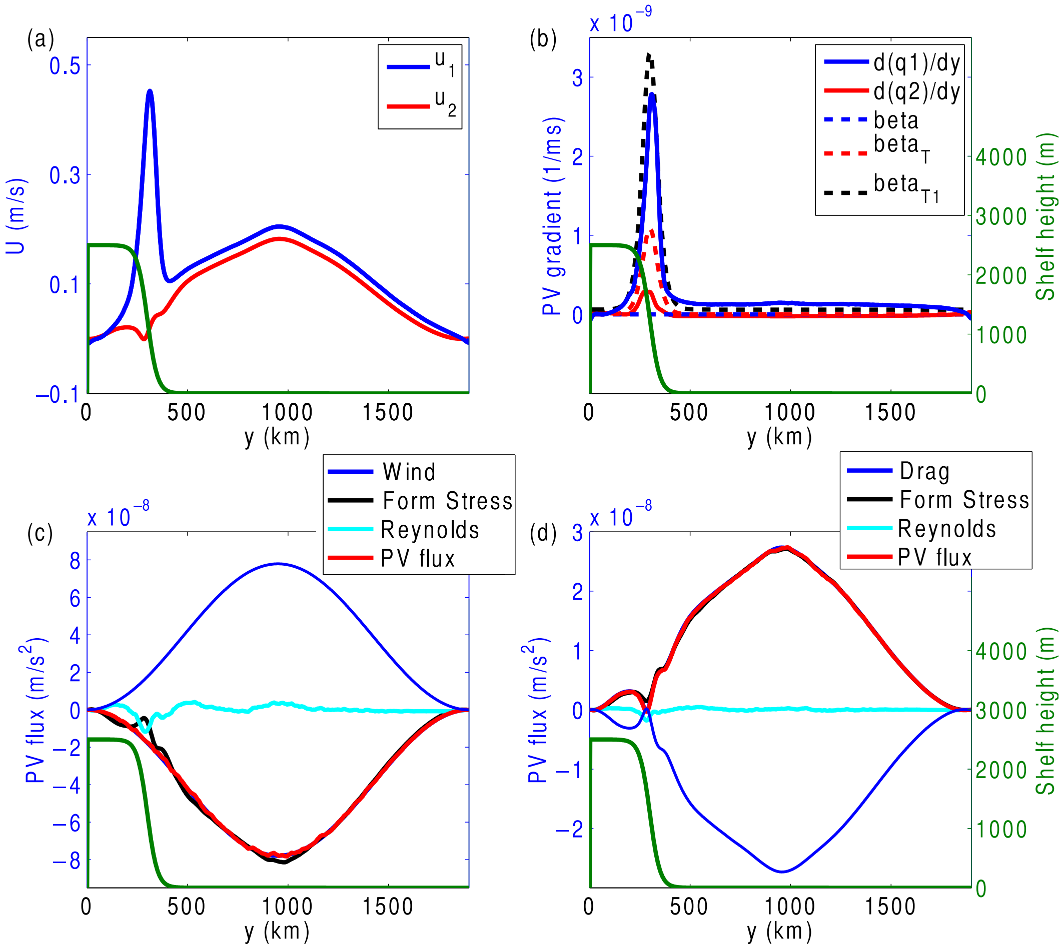

FIG. 8. (a) Time-averaged, zonally averaged velocity in the upper and lower layers. (b) Time-averaged zonally averaged meridional PV gradient in the upper and lower layers. The dashed lines show upper-layer background PV gradient β, the lower-layer background PV gradient β_T, and the analytic estimate for the upper-layer time-mean PV gradient β_{T1}. (c) Time-averaged, zonally averaged, upper-layer meridional PV flux $\overline{q_1'v_1'}$, Reynolds stress divergence $\overline{\psi_{1x}'\psi_{1yy}'}$, interfacial stress $F_1\overline{\psi_{1x}'\psi_2'}$, and the wind forcing $\overline{\tau}/(\rho H_1)$. (d) Time-averaged, zonally averaged, lower-layer meridional PV flux $\overline{q_2'v_2'}$, Reynolds stress divergence $\overline{\psi_{2x}'\psi_{2yy}'}$, interfacial stress $F_2\overline{\psi_{2x}'\psi_1'}$, and drag $-ru_{g2}$. The results in all four panels come from the reference simulation ($\tau_0 = 0.08\,\mathrm{N\,m^{-2}}$, $W = 50$ km). The green curve in all four panels shows the height of the bottom topography.

vertical shear, the jet remains close to the critical condition for baroclinic instability $\partial q_2/\partial y \sim 0$, which suggests that baroclinic processes are also key to describing its dynamics.

b. Steady state

Results obtained for the long time averaging of the reference simulation are shown in Fig. 8. Figure 8b shows that the maximum upper-layer PV gradient equals β_{T1}. This maximum coincides with the strong upper-layer jet observed over the shelf break in Fig. 8a. The lower-layer steady-state PV budget is shown in Fig. 8d, where the bottom drag at each latitude is balanced by the meridional eddy PV flux $\langle -\overline{v_{g2}'q_2'}\rangle = \langle -r\overline{u_2}\rangle$ [see Eq. (12)]. Here, $\langle\ \rangle$ signifies a time mean. The reduced lower-layer PV flux over the shelf break coincides with a curbing of the abyssal velocities and indicates a minimum in the cross-shelf exchange in the bottom layer because of the presence of the topography. On the other hand, Fig. 8c shows that the topography does not affect the time-averaged upper-layer meridional PV flux, which must balance the wind forcing at steady state: $\langle -\overline{v_{g1}'q_1'}\rangle = \tau^{(x)}/(\rho_1 H_1)$ [see Eq. (11)]. This implies that the long time-averaged upper-layer meridional eddy PV flux (and hence the total amount of upper-layer cross-shelf exchange) is independent of the bottom topography in this QG setup. The PV flux in each layer can be decomposed into the sum of the Reynolds stress divergence $\overline{\psi'_{kx}\psi'_{kyy}}$ and the interfacial form stress $F_k\overline{\psi'_{kx}\psi'_{k+1}}$. The lower-layer PV flux is dominated by the contribution of the form stress, while the Reynolds stress divergence is small (Fig. 8d). In the upper layer, a negative Reynolds stress divergence is observed over the center of the shelf break (Fig. 8c).

These time-averaged fields are consistent with the results of Zhang et al. (2011), who suggest that the creation of a shelf break is due to a local suppression of the form drag over the continental slope. Since the upper-layer PV flux must balance the wind forcing in steady state, the local suppression of the form drag results in an increased magnitude Reynolds stress divergence over the continental shelf break in the upper layer, which allows for the development of a shelfbreak jet. In the following, we show that this enhanced Reynolds stress divergence is only marginally observed on the flank of the jet during the stable growth period. However, a strong peak of the Reynolds stress divergence is observed during the jet instability and drifting, which suggests that different phases of the jet evolution must be considered independently, rather than in a time-averaged sense.

c. Shelfbreak jet life cycle

We now focus on the evolution of the zonal momentum budget during specific periods in the life cycle of a typical shelfbreak jet, from its formation to its destruction. In each layer, the dominant zonal momentum balance at statistical equilibrium is

$$\frac{\partial\langle\overline{u_1}\rangle}{\partial t} = 0 = \langle\overline{\psi'_{1x}\psi'_{1yy}}\rangle + F_1\langle\overline{\psi'_{1x}\psi'_2}\rangle + \frac{\langle\overline{\tau}\rangle}{\rho_1 H_1}, \quad \text{and} \qquad (16)$$

$$\frac{\partial\langle\overline{u_2}\rangle}{\partial t} = 0 = \langle\overline{\psi'_{2x}\psi'_{2yy}}\rangle + F_2\langle\overline{\psi'_{2x}\psi'_1}\rangle - r\langle\overline{u_2}\rangle, \qquad (17)$$

where the time-averaged Reynolds stress divergence and interfacial stress have to balance the upper-layer input by the wind and the lower-layer sink by the bottom drag. Together, the Reynolds stress divergence and the interfacial form stress equal the meridional PV flux $\overline{v'_k q'_k}$.

It is useful to distinguish three distinct stages of the shelfbreak jet cycle: 1) the growth of the jet, 2) the onset of baroclinic instability, and 3) its meridional drift. Figures 9a and 9b show Hovmöller diagrams of the upper- and lower-layer zonally averaged zonal velocity of a typical shelfbreak jet in the statistically equilibrated regime of the reference simulation. The times of each of the three stages are indicated by dashed lines on the Hovmöller diagrams. Instantaneous profiles of the different terms of the zonal momentum balance corresponding to these three stages are shown in panels (U1) to (U3) for the upper layer and (L1) to (L3) for the lower layer. Notice that Eqs. (16) and (17) hold only for long time averaging (see Fig. 8), such that the sum of the terms on the right-hand side of the equations do not add to zero in the profiles shown in Fig. 9. The instantaneous profile of the tendency in the zonal velocity is also shown in Fig. 9:

1) The first stage is characterized by the long period after an instability event, where a stable jet grows over the topographic slope. During this period, there is little eddy activity over the shelf break [see panels (U1) and (L1) of Fig. 9] and the meridional PV flux across the shelfbreak center remains close to zero in both layers. In the upper layer, the input of momentum by the wind accelerates the flow on the shelf break, where $\overline{v'_k q'_k} \sim 0$. This is in contrast with the flat bottom region north of the topographic slope, where the wind input is balanced mainly by interfacial form stress. This strengthens the PV barrier between the continental shelf and the flat bottom region up north.[8] In the lower layer [see panel (L1)], the contribution of the bottom drag slowly destroys the PV gradient over the shelf break.
2) The second stage occurs once the lower-layer PV gradient becomes negative at y_0 and the flow becomes baroclinically unstable. A peak of interfacial form stress centered on the shelfbreak jet now transfers zonal momentum downward from the upper layer to the lower layer [see (U2) and (L2) of Fig. 9]. This interfacial form stress is largely balanced by bottom drag in the lower layer and by Reynolds stress divergence in the upper layer, such that the velocity tendency is small and the vertical shear is essentially unchanged (see Fig. 5b). The convergence of Reynolds momentum flux in response to baroclinic stirring has been discussed extensively in the context of the midlatitude atmospheric jets (e.g., Vallis et al. 2004; Dritschel and McIntyre 2008).
3) In the third stage, the jet is drifting northward. In Fig. 9b, a velocity dipole is observed in the lower-layer zonal velocities; westward velocities are observed at the southern flank of the lower-layer jet, whereas eastward velocities occur at its northern flank. Snapshots of relative vorticity taken from this stage show that a train of coherent vortices develop over the shelf break (not shown). This wavelike behavior is strongest in the upper layer, where the PV gradients are largest. Associated with this dipole is a strong inversion of the Reynolds stress

---

[8] Recall from Fig. 7 that the PV barrier is only weakened (but not destroyed) by the previous instability event in a statistically equilibrated regime.

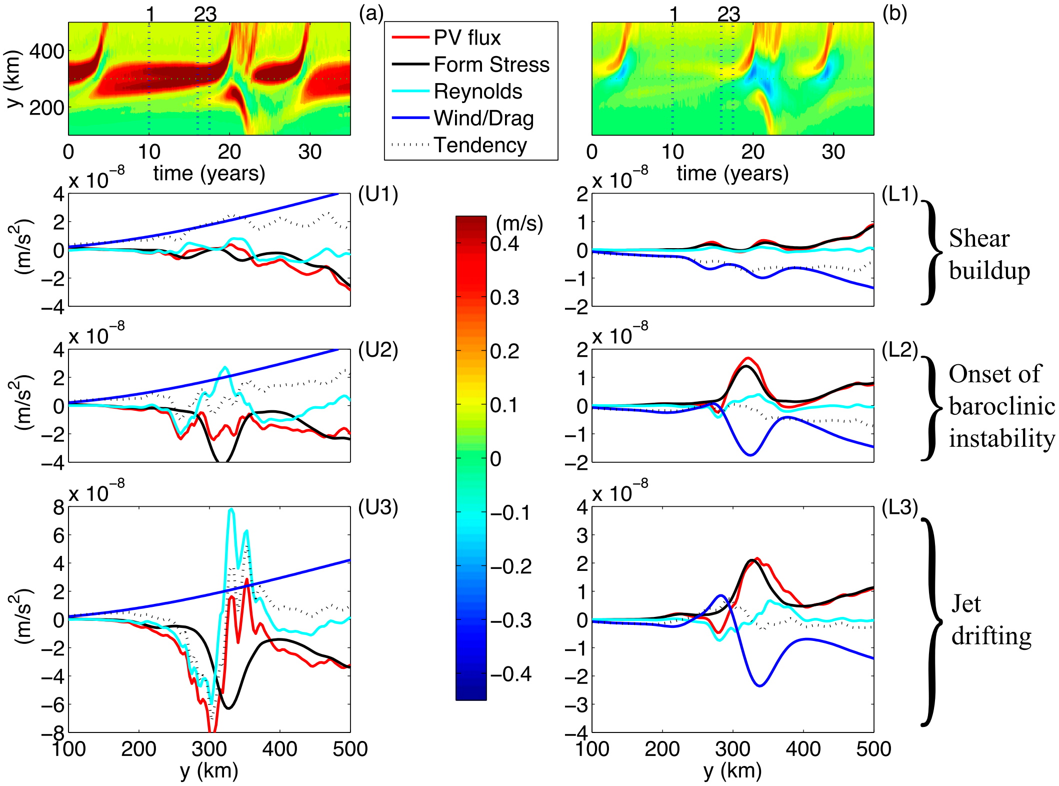

FIG. 9. (a) Hovmöller diagram of the upper-layer zonally averaged zonal velocity during a typical instability event for the reference simulation ($\tau_0 = 0.08\,\mathrm{N\,m^{-2}}$, $W = 50\,\mathrm{km}$). Instantaneous profiles of the upper-layer zonally averaged eddy PV flux, Reynolds stress divergence, interfacial stress, wind, and tendency of the zonal velocity for the three stages of the shelfbreak jet cycle are shown in (U1), (U2), and (U3). The times of these three instantaneous profiles are shown by dotted lines in (a). (b) (L1), (L2), and (L3) show the same fields as (a), (U1), (U2), and (U3), but for the lower layer, with drag instead of wind.

divergence across the jet in both layers [see Fig. 9, (U3) and (L3)]. This moves zonal momentum northward across the jet, decelerating its southern flank and accelerating its northern flank. This results in the northward drift of the zonal jet, which is the focus of the next section.

5. Meridional drifting of zonal jets

In the context of a stochastically forced barotropic system on a beta plane, Srinivasan (2014) observed that meridionally drifting jets occur when the forcing is anisotropic and also breaks reflectional symmetry. Here, in the context of our reference wind-driven setup, the effect of both the meridional curvature in the bottom topography and the meridional variation of the wind stress can result in an anisotropic eddy forcing that can break reflectional symmetry. To deconvolve the effect of wind and topography, experiments in this section are forced using a constant-imposed background shear, U_s in Eqs. (11) and (12), instead of using wind forcing. With this uniform forcing, only curvature in the topography can cause breaking of the reflectional symmetry.

In a first series of experiments, we set $\beta = 0$ but use the same hyperbolic tangent shelf as before [see Eq. (5)]. To avoid the interactions with the boundaries, the shelf break is shifted to the center of the domain $y_0 = L_y/2$. Figure 10 shows an example of an experiment forced with a uniform shear $U_s = 0.2\,\mathrm{m\,s^{-1}}$ and a shelfbreak width $W = 50\,\mathrm{km}$. Figure 10a shows the effective topographic beta $\beta_T = \beta + [(f_0/H_2)(\partial h_b/\partial y)]$, which sets the instability criteria, and Fig. 10b shows a Hovmöller diagram of the zonal-mean upper-layer zonal velocity in a statistically equilibrated regime. Zonal jets form over the shelf break, where large values of β_T allow for the development of strong vertical shear. As observed previously, these jets become unstable and drift aperiodically. However, there is no preferential drifting

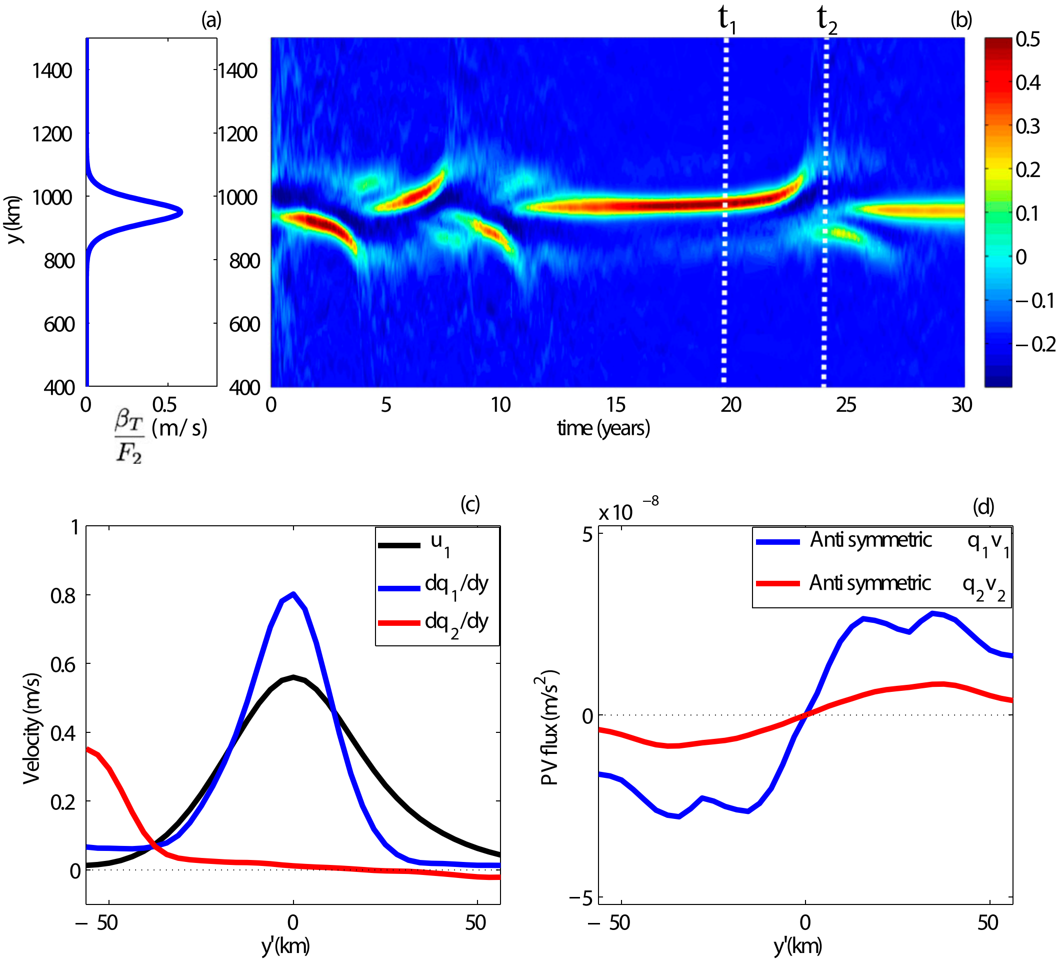

FIG. 10. (a) The instability threshold β_T/F_2 for a simulation with the shelf break at the center of the domain $y_0 = L_y/2$, shelfbreak width $W = 50$ km, forced by an imposed shear $U_s = 0.2\ \mathrm{m\,s^{-1}}$. (b) Hovmöller diagram of the upper-layer, zonally averaged zonal velocity for this simulation. The jets drift in both directions from regions of strong background PV gradient to regions of weak background PV gradient. (c) Time-averaged upper-layer velocity, upper-layer PV gradient, and lower-layer PV gradient of the jet that drifts between time t_1 and t_2, indicated by the dashed white lines in (b). (d) Asymmetric part of the upper- and lower-layer PV flux about the jet center. The time averaging in (c) and (d) is performed using a jet-following frame of reference $y'(t)$, such that the jet maximum is shifted to $y'(t) = 0$ for every individual snapshot contained in the average.

direction; northward and southward drifts are observed equally. Figure 10c shows the zonal-mean upper-layer zonal velocity and PV gradient averaged during the interval $t_1 < t < t_2$, where t_1 and t_2 are shown by dashed white lines in Fig. 10b. This time averaging is performed using a jet-following frame of reference $y'(t)$, such that the jet maximum is shifted to $y'(t) = 0$ for every individual snapshot contained in the average (Yoo and Lee 2010). The upper-layer velocity and PV gradient are approximately symmetric about the jet center, whereas the lower-layer PV gradient is clearly asymmetric about the jet center. Moreover, the lower-layer PV gradient becomes negative only on one side of the jet, which suggests that one side of the jet is more baroclinically unstable than the other.

To further investigate the impact of this asymmetry about the jet center, we consider the eddy PV fluxes over the same time period ($t_1 < t < t_2$). Figure 10d shows the asymmetric part of the upper- and lower-layer meridional eddy PV fluxes defined as

$$[\overline{q_i'v_i'}(y')]_{\mathrm{asym}} = \frac{\overline{q_i'v_i'}(y') - \overline{q_i'v_i'}(-y')}{2}\,. \qquad (18)$$

As was observed previously in the jet drifting section of Fig. 9, a strong inversion of the PV flux occurs across the jet in Fig. 10d, which tends to decelerate the flow on the southern flank of the jet and accelerate the flow on its northern flank, resulting in the meridional jet drift.

a. *Physical mechanism for the jet drifting*

Similar meridional jet drifting was reported by Thompson (2010) using a two-layer QG model with sinusoidal zonal ridges. In that study, the author suggests that meridional drift of a zonal jet can occur when the flanks of the jet feel different local PV gradients. This gives rise to baroclinic instability that is meridionally asymmetric about the jet center. In this view, a jet would always drift toward a more unstable latitude. We hypothesize that this same mechanism is responsible for meridional drift of zonal jets in our experimental setup. In the specific example of Fig. 10, the maximum condition for baroclinic instability $\max(\beta_T/F_2)$ occurs at the center of the shelf break $y_0 = L_y/2$ (which coincides with the center of the domain) and decreases symmetrically to the north and to the south. During the stable shear buildup period, the jet remains centered on the shelf break until the onset of baroclinic instability. We speculate that eddies developing from this instability perturb the jet, such that it is displaced from y_0. This can occur evenly to the north or south. Once the jet has shifted away from y_0 and one flank of the jet is more unstable than the other, the above drifting mechanism can operate: inversion of the Reynolds stress divergence across the jet decelerates one flank of the jet and accelerates the other. This would explain why there is no preferential drifting direction in the example of Fig. 10.

b. *The effect of the shelfbreak curvature on the drifting speed*

In the above setup, the asymmetric instability condition across the jet comes from differences in topographic slope between each flank of the jet. This corresponds to the curvature (or second derivative) of the topographic profile. More curvature implies more asymmetry, which should result in a higher drifting speed. We thus speculate that the curvature should modulate the meridional drifting speed. The curvature of the hyperbolic tangent shelf defined in Eq. (5) decreases with W. Figure 11 shows the average meridional jet drift velocity obtained for increasing values of the shelf curvature $Q = \partial^2 h_b/\partial y^2$ at $y = 1000\,\text{km}$. The average drift velocity is obtained by tracking the jet center during each northward drifting event and averaging the speed measured at a fixed latitude $y = 1000\,\text{km}$, which is 50 km north of the center of the shelf break. Notice that the magnitude of the drift velocity does not depend of the drifting direction, such that equivalent results are obtained with southward drifting events. Figure 11 shows that the average jet drift velocity increases with the topographic curvature for a fixed latitude, which supports the idea that drifting may be due to meridionally asymmetric baroclinic instability about the jet center.

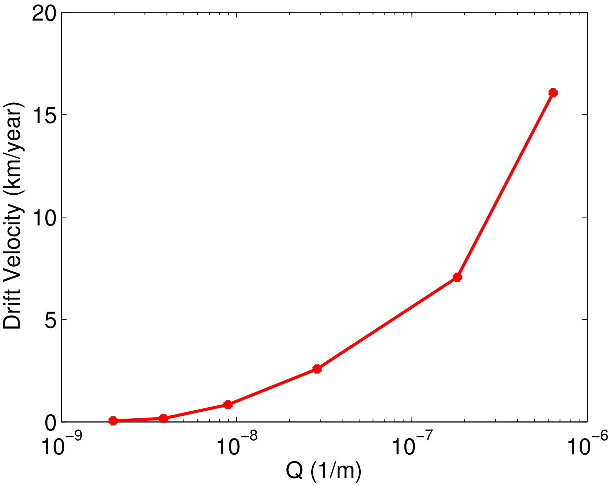

FIG. 11. The meridional jet drift velocity for different values of the topographic curvature $Q = \partial^2 h_b/\partial y^2$. The drift velocities are measured at y = 1000 km (50 km north of the center of the domain). Simulations were forced using a background shear $U_s = 0.2\,\text{m}\,\text{s}^{-1}$. The simulations used a hyperbolic tangent shelf described by Eq. (5), positioned in the center of the domain with $y_0 = L_y/2$.

EXPERIMENTS USING A CONSTANT CURVATURE

In the above experiments, curvature is not spatially uniform across the domain. Moreover, the local slope at $y = 1000\,\text{km}$, which determines the local value of the lower-layer PV gradient, varies throughout the experiments. Since for a given curvature, the drift speed may depend on the local topographic slope and on the local amount of eddy kinetic energy (EKE), we now study the case of a parabolic bottom topography, for which the curvature is constant across the domain. Simulations are performed using a parabolic bottom topography described by

$$h_b(y) = ay^2 + by, \tag{19}$$

where $a = Q/2$ and $b = [-(QL_y/2) - (h_0/2W)]$. In this set of experiments, we again set $\beta = 0$. Examples of different topographic profiles used in this series of experiment are shown in the inset of Fig. 12a. The topographic height at the southern boundary and the northern boundary are set to $h_b(0) = 0$ and $h_b(L_y) = -(h_0/2W)L_y$, respectively. By construction, the slope at the center of the domain is set to a constant value

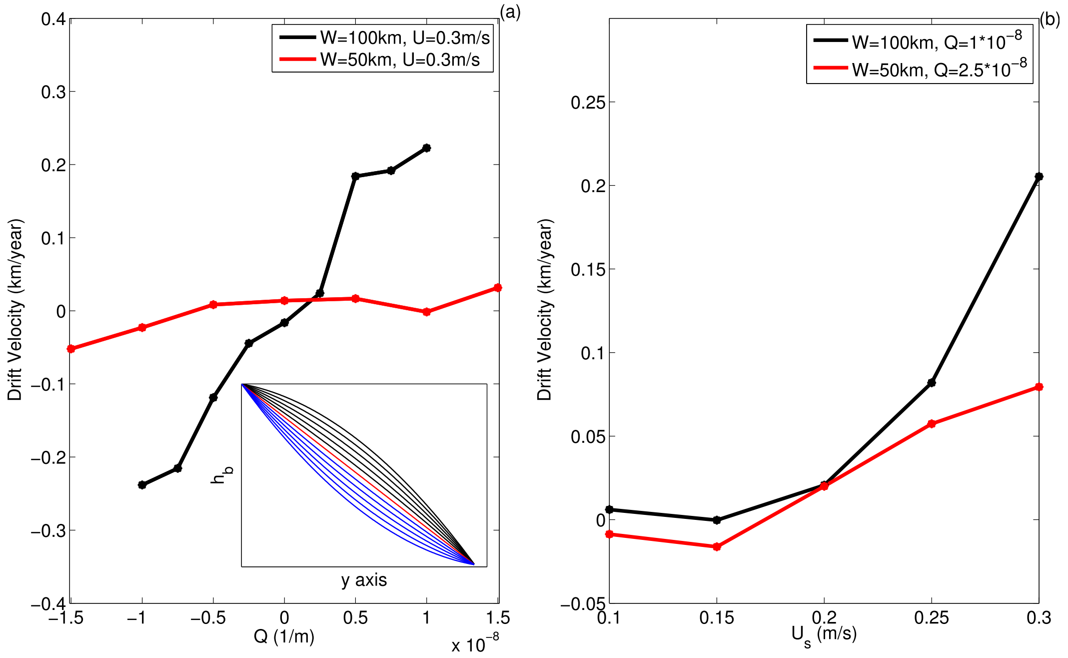

FIG. 12. (a) Meridional jet drifting velocity for different values of $Q = \partial^2 h_b/\partial y^2$ for simulations using shelfbreak widths $W = 100$ and 50 km, forced by an imposed shear $U_s = 0.3\,\mathrm{m\,s^{-1}}$. The jets drift northward for $Q > 0$ and southward for $Q < 0$. (b) Jet drifting velocity for different values of imposed shear U_s for simulations using shelfbreak widths $W = 100$ and 50 km and curvatures $Q = 10 \times 10^{-9}$ and $25 \times 10^{-9}\,\mathrm{m^{-1}}$. Both sets of simulations used a parabolic bottom topography. The inset in (a) shows an example of the parabolic bottom topography used. Topographies with $Q > 0$ are plotted in blue, $Q < 0$ are plotted in black, and $Q = 0$ (linear slope) is plotted in red.

$\partial[h_b(L_y/2)]/\partial y = -h_0/2W$, and this is where the jet drift speed is measured. As such, for a given U_s and W, all experiments should have the same local amount of EKE and same local slope at $y = L_y/2$, independent of the curvature Q. Only negative sloping topography is considered in these experiments, which limits the range of curvature to $|Q| < h_0/(WL_y)$.

Figure 12a shows the drifting velocity as a function of Q for two values of W: 50 and 100 km. Results agree broadly with the drifting mechanism described above; jets drift northward for $Q > 0$, southward for $Q < 0$, and drift is negligible for $Q = 0$. As such, jets always drift from regions of strong to regions of weak lower-layer background PV gradient, toward a more unstable region. In the range of parameter considered, the drifting speed varies approximately as a linear function of the curvature. For a fixed Q, the jet drift velocity decreases with the topographic slope (for decreasing W). For steep bottom slope ($W = 50$ km), topography stabilizes the flow such that it becomes only marginally unstable, and the drifting velocities remain close to zero. Figure 12b shows the drifting velocity as a function of the imposed background shear U_s for different values of W and Q. For fixed W and Q, the jet drifting speed increases with imposed background shear U_s, which suggests that the local value of EKE (set by the magnitude of the baroclinic instability) is also key to the drifting process.[9]

Finally, it is worth mentioning that drifting velocities can be amplified when the effect of the topographic curvature is combined with the effect of meridionally varying wind forcing. In a setup using wind forcing, the distribution of EKE is not uniform and follows broadly the wind profile. In this context, we observed that meridionally varying wind forcing alone can induce jet drifting from regions of low EKE to regions of high EKE (not shown). This can be explained following the same argument as the one given above: jets are drifting toward a more unstable latitude. For example, in the reference setup of section 3, multiple zonal jets are observed in the instantaneous velocity fields north of the shelf break, which drift toward the center of the domain, where the EKE is maximal. These jets cannot be clearly made out in the Hovmöller diagram of zonally averaged zonal velocity (Fig. 7a). Over the continental shelf break, the combined effect of topography (creating a

---

[9] Note that the critical shear for instability at $y = L_y/2$ is $U_c = 0.58\,\mathrm{m\,s^{-1}}$ when $W = 50$ km and $U_c = 0.29\,\mathrm{m\,s^{-1}}$ when $W = 100$ km.

meridional gradient of the condition for baroclinic instability) and wind (inducing a meridional gradient of EKE) leads to drifting velocities that are much higher than those shown in Fig. 12.

c. *Mixing and drifting*

We end this section by discussing the possible link between the drifting of the jet and the mixing associated with an instability event. Using a uniform-imposed shear on a beta-plane QG setup, Pavan and Held (1996) showed that for a fixed β, eddy diffusivities increase with vertical shear following approximately U_s^3. They further showed that the diffusivities are strongly suppressed for increasing β. Here, in a context where β_T varies latitudinally, we speculate that a jet accumulating strong vertical shear over the shelf break (where β_T is large) and drifting quickly toward a flat bottom region (where β_T is small) can lead to high local values of eddy diffusivity. In this view, the effect of locally suppressed diffusivity over the shelf break would be compensated by the mixing associated with the drifting of the jet into a region of small β_T, where strong vertical shear leads to enhanced diffusivity. This could also explain the result observed in section 3 that the magnitude of a given cross-shelf mixing event is closely related to the vertical shear recorded over the shelf break before this event.

6. Experiments using a primitive equation model

In the following, we validate the use of the QG model by comparing some of its key results to a PE model. Although the QG model has been observed to be valid outside of its strict asymptotic regime (Williams et al. 2010; Poulin et al. 2014), it is unclear a priori if its use is justified in the context of large-amplitude topography like the one used in this work. However, results show that the QG model shares many of the important features with the PE model in a similar experimental setup.

a. *Primitive equation model*

A series of numerical experiments were carried out using MITgcm (Marshall et al. 1997a,b) with a similar experimental setup as the one used in the QG simulations above. The model used a horizontal resolution of $\Delta x = 2.5$ km and 25 vertical levels with layer thicknesses ranging from 30 m at the surface to 109 m at the bottom. The model geometry is a zonally reentrant channel with length $\hat{L}_x = 1050$ km, width $\hat{L}_y = 2100$ km, and depth $H = 2000$ m. The model topography is the same as in the QG setup and is described by Eq. (5) with the shelfbreak center at $y_0 = 300$ km and a shelf height $h_0 = 1500$ m. The flow was forced by the sinusoidal wind stress described by Eq. (6). No buoyancy flux is applied at the surface, similar to the QG simulations. Stratification is initialized to an exponential density profile given by $\rho(z) = \rho_0 \exp(z/D)$, defined using a linear equation of state with thermal expansion coefficient $\alpha = 2 \times 10^{-4}\,\mathrm{K}^{-1}$. The *e*-folding scale D was chosen such that the average steady-state deformation radius was $L_d = 12.9$ km, away from the shelf break. The model was spun up until the integrated zonal transport and the domain-averaged eddy kinetic energy converged. The steady-state domain-averaged deformation radius was found to remain close to its initial value despite latitudinal variation in the stratification caused by sloping isopycnals. Note also that the stratification over the continental shelf was found to be sensitive to changes in the shelfbreak width parameter W.

The K-profile parameterization (KPP) was used to account for vertical mixing (Large et al. 1994). Biharmonic momentum dissipation was used with a hyperviscosity $\widetilde{A_H} = 5\,\mathrm{m}^4\,\mathrm{s}^{-1}$. A linear bottom drag was used with a bottom drag coefficient $r = 2 \times 10^{-4}\,\mathrm{s}^{-1}$.

b. *Phenomenology*

Figure 13 shows the Hovmöller diagrams of the zonal-mean zonal surface velocity for various values of the shelfbreak width W for simulations using $\tau_0 = 0.08\,\mathrm{N\,m}^{-2}$. Only the southern half of the domain is shown. Results are qualitatively similar to those found using the QG model. Three distinct parameter regimes, similar to those discussed in section 3, are observed: (i) for narrow shelfbreak widths, no jet forms over the shelf break; (ii) for shelves of intermediate width, we observe a unique shelfbreak jet that remains stationary for a number of years before becoming unstable and drifting away from the shelf break; and (iii) for larger W, multiple jets form over the shelf break and constantly drift northward.

Figure 14 shows that the maximum vertical shear observed over the shelfbreak center is also strongly dependent on W. Vertical shear is small for narrow shelf breaks, maximum for shelves of intermediate width, and decreasing with W for wide shelves. This figure is readily comparable to Fig. 3a, which shows a similar result using the QG model.

Figure 15 shows different time series relevant to the shelfbreak jet life cycle for a simulation using $W = 50$ km and $\tau_0 = 0.08\,\mathrm{N\,m}^{-2}$ in the one jet regime. Figure 15a shows the Hovmöller diagram of the zonal-mean zonal surface velocity, while Fig. 15b shows a time series of the vertical shear averaged over the shelfbreak region. Only the southern part of the domain is displayed in the Hovmöller diagram in Fig. 15a. The vertical shear accumulates over a long period during which the jet is stable. This is followed by a sharp decrease in shear, as the jet begins to drift.

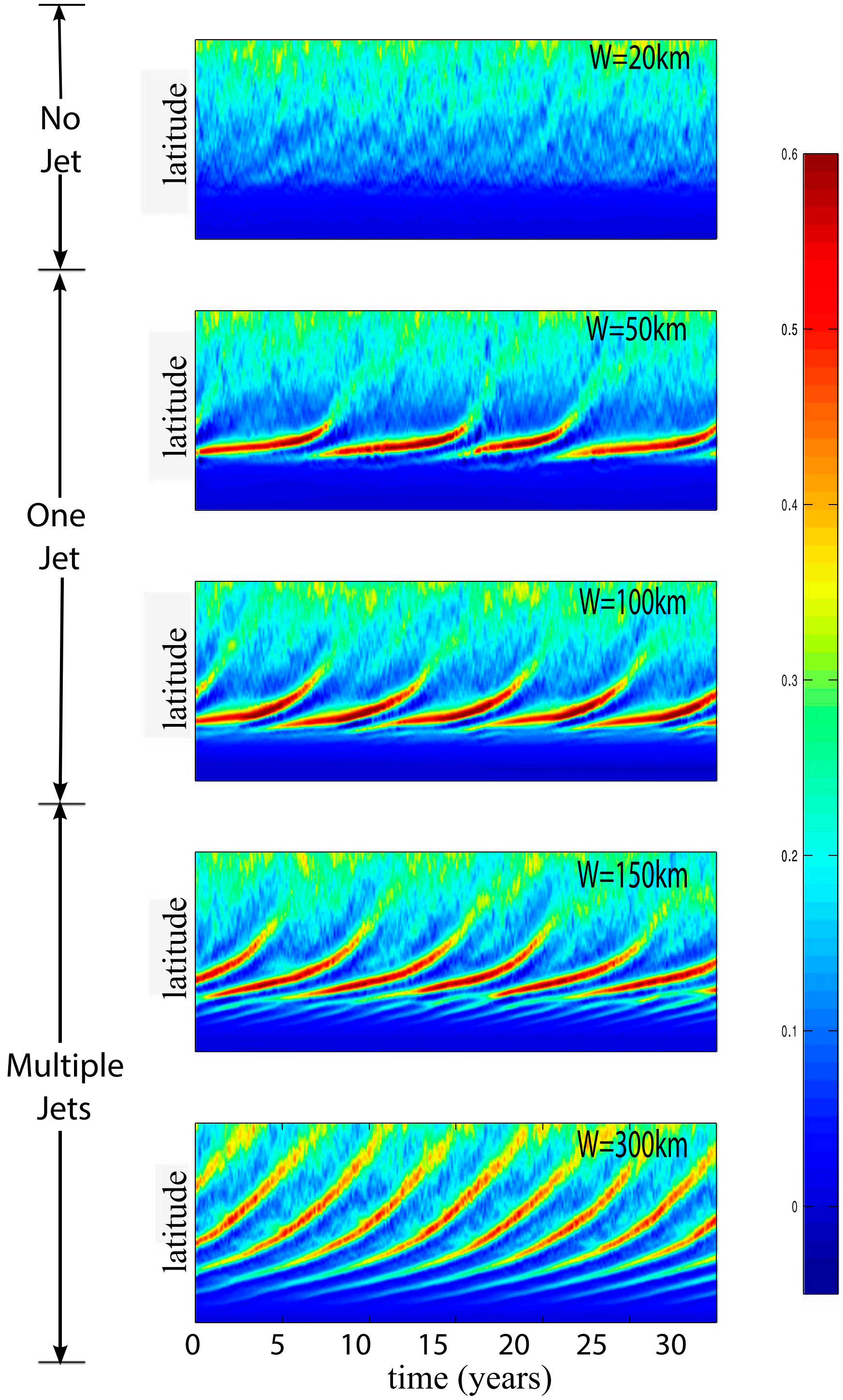

FIG. 13. Hovmöller diagrams of the zonally averaged zonal velocity at the surface are shown for different shelfbreak widths. (top to bottom) Shelfbreak widths $W = 20, 50, 100, 150$, and 300 km are shown. The simulations are performed using MITgcm primitive equation model. Only the southern half of the domain is shown.

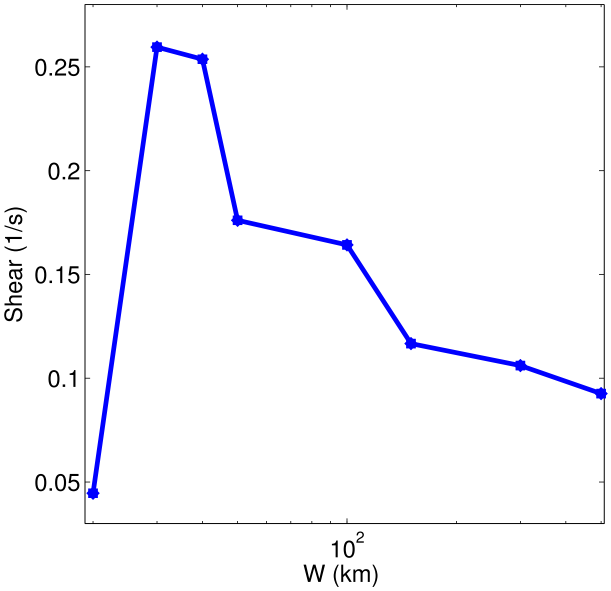

FIG. 14. Maximum vertical shear observed over the continental shelfbreak region for model simulations using different shelfbreak widths W. This figure made using results from the primitive equation model.

Similar to what was observed in the QG model, the drifting of the jet is associated with increased eddy activity and cross-shelf mixing. Figures 15c to 15f show time series of the zonally averaged EKE $0.5[(u')^2 + (v')^2]$ and meridional eddy PV flux[10] $\overline{v'q'}$ averaged over the shelfbreak region. Figures 15c and 15e show time series of the EKE and PV flux at the surface, while Figs. 15d and 15f show Hovmöller diagrams of these quantities as a function of depth (only the top 1200 m of the water column are shown). The magnitude of the EKE and PV flux are weak during periods where the jet is stable but increase significantly when the jet drifts. This enhanced eddy activity suggests that the drifting is caused by an instability of the jet. Moreover, the strongly negative PV flux associated with this instability event indicates elevated cross-shelf mixing during this period. Figures 15d and 15f show that both the EKE and PV flux have the largest magnitudes near the surface during instability events, consistent with the choice of an exponential density profile. This suggests that a two-layer representation can capture the first-order dynamics of this system. In summary, the strong similarities between the PE simulations and the QG simulations give us further confidence that QG dynamics can be used to interpret more realistic shelfbreak jets.

7. Conclusions

This work describes the effect of the dynamics of topographically steered zonal jets on the mixing across an idealized continental shelf break of the West Antarctica Peninsula. The relationship between the temporal variability of the cross-shelf exchange and the instability and drifting of the shelfbreak jets is examined in a series of quasigeostrophic and primitive equation numerical experiments. First, by varying the width of a 2500-m-high zonally symmetric hyperbolic tangent topography, we show that the state of the shelfbreak flow can be classified in terms of its proximity to the condition for baroclinic instability: (i) For a shelfbreak width smaller than the eddy scale, the shelfbreak flow is subcritical and no jet is observed on the topographic slope. (ii) For a shelfbreak width slightly greater than the eddy scale, a strong jet develops that becomes intermittently unstable and drifts away from the shelf break whenever the vertical shear reaches the critical condition for baroclinic instability. (iii) For a wide shelf with weaker topographic slope, the shelfbreak flow is critical to supercritical and multiple jets drifting meridionally are observed on the shelf break.

Our focus is on the regime where the shelfbreak width is slightly bigger than the eddy scale, for which the cross-shelf mixing associated with instability events is maximal. Spinup of the channel from rest shows a much longer equilibration time for the shelfbreak flow than for the flat bottomed region farther north. During this equilibrium time, a sharp upper-layer PV barrier forms over the shelf break. The magnitude of this upper-layer PV gradient sets the magnitude of the upper-layer jet and corresponds to the gradient of the background barotropic geostrophic contours. At statistical equilibrium, the shelfbreak jet displays a low-frequency intermittent variability. The shelfbreak jet life cycle can be divided in three main steps: 1) a stable growth period during which vertical shear accumulates over the shelf break; 2) the onset of baroclinic instability during which the vertical shear is maintained by the combined effect of the Reynolds stress divergence in the upper layer and bottom friction in the lower layer; and 3) a meridional drift period during which a strong inversion of the Reynolds stress divergence across the jet accelerates one side of the jet and decelerates the other, forcing it to move away from the shelf break. We then speculate that the meridional drift of the shelfbreak jet is because of the meridional asymmetry of the baroclinic instability about the jet center, similar to the results of Thompson (2010),

---

[10] The Ertel PV is defined as $q = \omega_a \cdot \nabla S$, where ω_a is the absolute vorticity and S is the stratification, defined as $S = b + N^2 z$, where b is the buoyancy of the fluid and N is the Brunt–Vaisala frequency (Müller 1995).

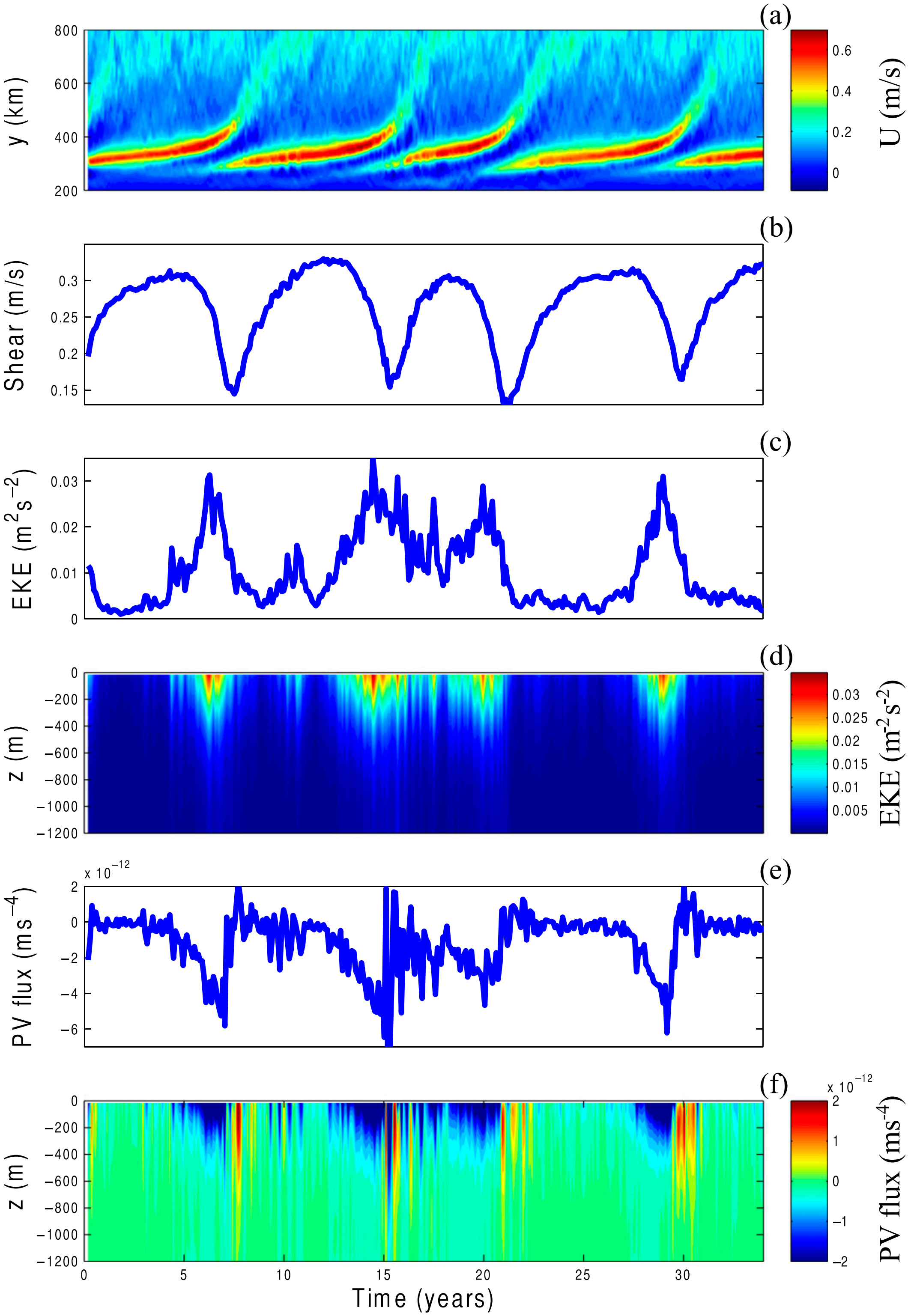

FIG. 15. Results from a PE model simulation with wind forcing $\tau_0 = 0.04\,\mathrm{N\,m^{-2}}$ and shelfbreak width $W = 50\,\mathrm{km}$. (a) Hovmöller diagram for the zonally averaged surface zonal velocity in the southern half of the domain. (b) Time series of the vertical shear in the zonal velocity averaged over the shelfbreak region. The zonally averaged (c) EKE and (e) PV flux at the surface, averaged over the shelfbreak region. Hovmöller diagrams of the (d) zonally averaged EKE and (f) PV flux at different depths averaged over the shelfbreak region. Quantities shown in (b)–(f) are averaged between $y = 280$ and 320 km.

observed in the context of braided jets over sinusoidal topography. Here, we show that jet drifting can occur for isolated jets and does not involve jet interaction. We also demonstrate that jet drifting is a distinct stage in the jet life cycle and occurs only after the onset of baroclinic instability. Finally, we systematically investigate this mechanism in experiments using uniform-imposed shear and varying curvature of a parabolic topographic profile.

Our numerical simulations neglected two important aspects of the shelfbreak dynamics that are the focus of ongoing research. First, the simulations did not include zonally asymmetric topography, especially canyons, that is known to be important for cross-shelf mixing (Zhang et al. 2011; St-Laurent et al. 2013). In a QG setup with a zonally sinusoidal shelf break, preliminary results show that a mechanism involving shear buildup, instability, and drifting of the shelfbreak jet is also observed with zonally asymmetric topography. However, our results also suggest that the cross-shelf exchange is influenced by the wavelength of the shelfbreak undulations. For a shelfbreak wavelength comparable to the eddy scale, jets do not develop on the topography, and cross-shelf mixing is strongly enhanced. Note that the larger-scale zonal asymmetry of the ACC can also affect the velocity and stratification over the WAP continental shelf, making some of the regimes described in this study impossible to observe in the real ocean. A second drawback of our experimental setup is that it does not address the effect of meridionally varying stratification across the shelf break, since the QG framework assumes a constant deformation scale (and hence stratification) in the entire domain. Preliminary simulations using a primitive equation model show that the shelfbreak jet dynamics are very sensitive to the southern boundary condition setting the stratification over the continental shelf. However, strong similarities between the results of the QG model and those of a more realistic primitive equation model suggest that the shelfbreak jet behavior described in this study may account for a first-order representation of the observed jet behavior over the WAP continental shelf break.

Acknowledgments. Funding for this research was provided by NYU Abu Dhabi Grant G1204 and the National Science Foundation Grants NSF DMS-0940241 and NSF ANT-0732869.

APPENDIX

Mass and Momentum Conservation in the Quasigeostrophic Numerical Model

Mass conservation is achieved by imposing

$$\int_0^{L_y}\int_0^{L_x}\psi_k\,dx\,dy = 0 \qquad \text{(A1)}$$

in each layer. Here, $k = [1, 2]$ stands for upper and lower layer, and L_x and L_y are the channel length and width, respectively. Conservation of momentum is achieved using the zonal momentum equation integrated over a latitude circle in the channel (McWilliams 1977)

$$\oint_0^{Lx}\left[D_t(u_{gk}) - f_0 v_{ak} - \beta y v_{gk} = -\delta_{2,k} r u_{gk} - A_H\nabla^4 u_{gk} + \delta_{1,k}\frac{\tau}{\rho_1 H_1}\right]dx, \qquad \text{(A2)}$$

where $\delta_{i,j}$ is the Kronecker delta function, and $u_g = -\partial\psi/\partial y$ and $v_g = \partial\psi/\partial x$ are the first-order geostrophic horizontal velocities. The interface displacement at the surface and between the layers is given by $\eta_0 = (f_0\psi_1)/g$ and $\eta_1 = [f_0(\psi_2 - \psi_1)]/g'$, respectively.

To isolate the ageostrophic velocity, v_a in Eq. (A2), we use the mass flux conservation across a latitude circle in channel

$$\oint_0^{Lx}[(H_k v_{ak}) - v_{gk}(\eta_k - \eta_{k-1})]\,dx = -\frac{d}{dt}\iint_A(\eta_k - \eta_{k-1})\,dx\,dy, \qquad \text{(A3)}$$

where A is the area of the region south of the latitude circle.

REFERENCES

Benilov, E. S., 2001: Baroclinic instability of two-layer flows over one-dimensional bottom topography. *J. Phys. Oceanogr.,* **31,** 2019–2025, doi:10.1175/1520-0485(2001)031<2019:BIOTLF>2.0.CO;2.

Blumsack, S. L., and P. J. Gierasch, 1972: Mars: The effects of topography on baroclinic instability. *J. Atmos. Sci.,* **29,** 1081–1089, doi:10.1175/1520-0469(1972)029<1081:MTEOTO>2.0.CO;2.

Boland, E. J. D., A. F. Thompson, E. Shuckburgh, and P. H. Haynes, 2012: The formation of nonzonal jets over sloped topography. *J. Phys. Oceanogr.,* **42,** 1635–1651, doi:10.1175/JPO-D-11-0152.1.

Chen, C., and I. Kamenkovich, 2013: Effects of topography on baroclinic instability. *J. Phys. Oceanogr.,* **43,** 790–804, doi:10.1175/JPO-D-12-0145.1.

Dinniman, M. S., and J. M. Klinck, 2004: A model study of circulation and cross-shelf exchange on the West Antarctic Peninsula continental shelf. *Deep-Sea Res.,* **51,** 2003–2022, doi:10.1016/j.dsr2.2004.07.030.

——, ——, and W. O. Smith Jr., 2011: A model study of Circumpolar Deep Water on the West Antarctic Peninsula and Ross Sea continental shelves. *Deep-Sea Res. II,* **58,** 1508–1523, doi:10.1016/j.dsr2.2010.11.013.

——, ——, and E. E. Hofmann, 2012: Sensitivity of Circumpolar Deep Water transport and ice shelf basal melt along the West Antarctic Peninsula to changes in the winds. *J. Climate,* **25,** 4799–4816, doi:10.1175/JCLI-D-11-00307.1.

Dritschel, D. G., and M. E. McIntyre, 2008: Multiple jets as PV staircases: The Phillips effect and the resilience of eddy-transport barriers. *J. Atmos. Sci.,* **65,** 855–874, doi:10.1175/2007JAS2227.1.

Farrell, B. F., and P. J. Ioannou, 2003: Structural stability of turbulent jets. *J. Atmos. Sci.,* **60,** 2101–2118, doi:10.1175/1520-0469(2003)060<2101:SSOTJ>2.0.CO;2.

Hart, J. E., 1975: Baroclinic instability over a slope. Part I: Linear theory. *J. Phys. Oceanogr.,* **5,** 625–633, doi:10.1175/1520-0485(1975)005<0625:BIOASP>2.0.CO;2.

Hofmann, E. E., P. H. Wiebe, D. P. Costa, and J. J. Torres, 2004: An overview of the Southern Ocean Global Ocean Ecosystems Dynamics Program. *Deep Sea Res. II,* **51,** 1921–1924, doi:10.1016/j.dsr2.2004.08.007.

Irwin, R. L., and F. J. Poulin, 2014: The influence of stratification on the instabilities in an idealized two-layer ocean model. *J. Phys. Oceanogr.,* **44,** 2718–2738, doi:10.1175/JPO-D-13-0280.1.

Jacobs, S. S., 1991: On the nature and significance of the Antarctic slope front. *Mar. Chem.,* **35,** 9–24, doi:10.1016/S0304-4203(09)90005-6.

Jenkins, A., and S. Jacobs, 2008: Circulation and melting beneath George VI ice shelf, Antarctica. *J. Geophys. Res. Oceans,* **113,** C04013, doi:10.1029/2007JC004449.

Johnson, G. C., and H. L. Bryden, 1989: On the size of the Antarctic Circumpolar Current. *Deep-Sea Res.,* **36,** 39–53, doi:10.1016/0198-0149(89)90017-4.

Klinck, J. M., E. E. Hofmann, R. C. Beardsley, B. Salihoglu, and S. Howard, 2004: Water-mass properties and circulation on the West Antarctic Peninsula continental shelf in austral fall and winter 2001. *Deep-Sea Res. II,* **51,** 1925–1946, doi:10.1016/j.dsr2.2004.08.001.

Large, W. G., J. C. McWilliams, and S. C. Doney, 1994: Oceanic vertical mixing: A review and a model with a nonlocal boundary layer parameterization. *Rev. Geophys.,* **32,** 363–403, doi:10.1029/94RG01872.

Marshall, J., A. Adcroft, C. Hill, L. Perelman, and C. Heisey, 1997a: A finite-volume, incompressible Navier Stokes model for studies of the ocean on parallel computers. *J. Geophys. Res.,* **102,** 5753–5766, doi:10.1029/96JC02775.

——, C. Hill, L. Perelman, and A. Adcroft, 1997b: Hydrostatic, quasi-hydrostatic, and nonhydrostatic ocean modeling. *J. Geophys. Res.,* **102,** 5733–5752, doi:10.1029/96JC02776.

McWilliams, J. C., 1977: A note on a consistent quasigeostrophic model in a multiply connected domain. *Dyn. Atmos. Oceans,* **1,** 427–441, doi:10.1016/0377-0265(77)90002-1.

Moffat, C., R. C. Beardsley, B. Owens, and N. van Lipzig, 2008: A first description of the Antarctic Peninsula coastal current. *Deep-Sea Res. II,* **55,** 277–293, doi:10.1016/j.dsr2.2007.10.003.

——, B. Owens, and R. C. Beardsley, 2009: On the characteristics of Circumpolar Deep Water intrusions to the West Antarctic Peninsula continental shelf. *J. Geophys. Res.,* **114,** C05017, doi:10.1029/2008JC004955.

Müller, P., 1995: Ertel's potential vorticity theorem in physical oceanography. *Rev. Geophys.,* **33,** 67–97, doi:10.1029/94RG03215.

Nadeau, L. P., and D. N. Straub, 2012: Influence of wind stress, wind stress curl, and bottom friction on the transport of a model Antarctic Circumpolar Current. *J. Phys. Oceanogr.,* **42,** 207–222, doi:10.1175/JPO-D-11-058.1.

Orsi, A. H., T. Whitworth, and W. D. Nowlin, 1995: On the meridional extent and fronts of the Antarctic Circumpolar Current. Deep-Sea Res., **42,** 641–673, doi:10.1016/0967-0637(95)00021-W.

Pavan, V., and I. M. Held, 1996: The diffusive approximation for eddy fluxes in baroclinically unstable jets. *J. Atmos. Sci.,* **53,** 1262–1272, doi:10.1175/1520-0469(1996)053<1262:TDAFEF>2.0.CO;2.

Pedlosky, J., 1979: *Geophysical Fluid Dynamics.* Springer-Verlag, 624 pp.

Phillips, N. A., 1954: Energy transformations and meridional circulations. *Tellus,* **6A,** 273–286, doi:10.1111/j.2153-3490.1954.tb01123.x.

Poulin, F. J., and G. R. Flierl, 2005: The influence of topography on the stability of jets. *J. Phys. Oceanogr.,* **35,** 811–825, doi:10.1175/JPO2719.1.

——, A. Stegner, M. Hernndez-Arencibia, A. Marrero-Daz, and P. Sangrá, 2014: Steep shelf stabilization of the coastal Bransfield Current: Linear stability analysis. *J. Phys. Oceanogr.,* **44,** 714–732, doi:10.1175/JPO-D-13-0158.1.

Rhines, P. B., 1975: Waves and turbulence on a beta-plane. *J. Fluid Mech.,* **69,** 417–443, doi:10.1017/S0022112075001504.

Sinha, B., and K. J. Richards, 1999: Jet structure and scaling in Southern Ocean models. *J. Phys. Oceanogr.,* **29,** 1143–1155, doi:10.1175/1520-0485(1999)029<1143:JSASIS>2.0.CO;2.

Smith, D. A., and J. M. Klinck, 2002: Water properties on the West Antarctic Peninsula continental shelf: A model study of effects of surface fluxes and sea ice. *Deep-Sea Res. II,* **49,** 4863–4886, doi:10.1016/S0967-0645(02)00163-7.

Sokolov, S., and S. R. Rintoul, 2007: Multiple jets of the Antarctic Circumpolar Current south of Australia. *J. Phys. Oceanogr.,* **37,** 1394–1412, doi:10.1175/JPO3111.1.

Srinivasan, K., 2014: Stochastically forced zonal flows. Ph.D. thesis, Scripps Institution of Oceanography, University of California, San Diego, 76–95.

——, and W. R. Young, 2012: Zonostrophic instability. *J. Atmos. Sci.,* **69,** 1633–1656, doi:10.1175/JAS-D-11-0200.1.

St-Laurent, P., J. M. Klinck, and M. S. Dinniman, 2013: On the role of coastal troughs in the circulation of warm Circumpolar Deep Water on Antarctic shelves. *J. Phys. Oceanogr.,* **43,** 51–64, doi:10.1175/JPO-D-11-0237.1.

Thompson, A. F., 2010: Jet formation and evolution in baroclinic turbulence with simple topography by an open-ocean current. *J. Phys. Oceanogr.,* **40,** 257–278, doi:10.1175/2009JPO4218.1.

——, and K. J. Richards, 2011: Low frequency variability of Southern Ocean jets. *J. Geophys. Res.,* **116,** C09022, doi:10.1029/2010JC006749.

Vallis, G. K., E. P. Gerber, P. J. Kushner, and B. A. Cash, 2004: A mechanism and simple dynamical model of the North Atlantic Oscillation and annular modes. *J. Atmos. Sci.,* **61,** 264–280, doi:10.1175/1520-0469(2004)061<0264:AMASDM>2.0.CO;2.

Whitworth, T., A. H. Orsi, S. J. Kim, W. D. Nowlin, and R. A. Locarnini, 1998: Water masses and mixing near the Antarctic slope front. *Ocean, Ice, and Atmosphere: Interactions at the Antarctic Continental Margin, Geophys. Monogr.,* Vol. 75, Amer. Geophys. Union, 1–27, doi:10.1029/AR075p0001.

Williams, P. D., P. L. Read, and T. W. N. Haine, 2010: Testing the limits of quasi-geostrophic theory: Application to observed laboratory flows outside of the quasi-geostrophic regime. *J. Fluid Mech.,* **649,** 187–203, doi:10.1017/S0022112009993405.

Yoo, C., and S. Lee, 2010: Persistent multiple jets and PV staircase. *J. Atmos. Sci.,* **67,** 2279–2295, doi:10.1175/2010JAS3326.1.

Zhang, Y., J. Pedlosky, and G. R. Flierl, 2011: Cross-shelf and out-of-bay transport driven by an open-ocean current. *J. Phys. Oceanogr.,* **41,** 2168–2186, doi:10.1175/JPO-D-11-08.1.